Quantum Physics and Quantum Information with Atoms, Photons, Electrical Circuits, and Spins

Patrice Bertet

Université Pierre-et-Marie-Curie

Mémoire d'Habilitation à Diriger des Recherches

Quantum Physics and Quantum Information with Atoms, Photons, Electrical Circuits, and Spins

présenté par:
Patrice BERTET
(Groupe Quantronique, SPEC, CEA Saclay)

soutenu au CEA Saclay le 17 juin 2014 devant le jury composé de

Pr. Daniel ESTEVE	Examinateur
Pr. Ronald HANSON	Rapporteur
Pr. Hans MOOIJ	Examinateur
Pr. Jean-Michel RAIMOND	Examinateur
Pr. Andreas WALLRAFF	Rapporteur
Pr. Wolfgang WERNSDORFER	Rapporteur

Contents

Chapter 1

Introduction: From quantum paradoxes to quantum devices

1.1 The second quantum revolution

Research in quantum physics has undergone a major breakthrough since the years 1980s, when it became possible to manipulate and readout the state of individual quantum systems, thanks to the progress of various experimental techniques. One important motivation was *to test and to illustrate quantum theory at the level of individual systems*, where its most counter-intuitive aspects become most vividly apparent: entanglement, quantum measurement, .. With the advent of ion trapping, laser cooling, and parametric down-conversion, single ions, single photons could be detected and prepared into exotic quantum states. Two of the pioneers of this second quantum revolution were awarded the Nobel prize in 2012 : David Wineland for experiments with individual trapped ions, and Serge Haroche for experiments with single atoms interacting with single photons in a microwave cavity.

More recently, a new motivation has emerged for quantum state engineering of individual systems, in the direction of what could be described as applied quantum physics. The idea is to make use of the non-classical phenomena arising in quantum mechanics (such as entanglement or large-scale quantum state superpositions), to achieve certain tasks more efficiently than allowed by classical physics. In particular, a large effort worldwide is dedicated to building a quantum computer, that could outperform classical computers for certain problems thanks to entanglement and massive parallelism enabled by the superposition principle. A quantum computer relies on registers of quantum bits or qubits, which are two-level systems behaving quantum-mechanically. The qubits have to be initialized, prepared in arbitrary superpositions of entangled states, and read-out with high fidelity. Other interesting direction of applied quantum physics include quantum simulators, quantum metrology and sensing.

This field of both fundamental and applied quantum physics forms the research background of all my work, from PhD until now, and of my ongoing and future research projects. Within this well-identified conceptual framework, I have been led to work with a variety of quantum systems : atoms, electrical circuits, spins in crystals. Another central concept of all my research is the *strong coupling between light and matter*. Indeed, in order to produce interesting entangled states involving several of these systems, they need to be brought in interaction. This is most conveniently

achieved by exchanging real or virtual photons (at microwave frequencies in all the experiments reported here); but this is only possible if these photons are trapped for a sufficiently long time in a resonator to be emitted and re-absorbed coherently. The light-matter coupling thus needs to be much stronger than any dissipative process. One of my research contributions was precisely to extend the range of systems in which this strong coupling regime is reached.

1.2 From cavity to circuit QED

In the first part of this manuscript, I will give a brief account of my PhD and postdoc work. I did my PhD in the group of Serge Haroche at the Laboratoire Kastler-Brossel (ENS Paris), under the supervision of Jean-Michel Raimond. The experiment deals with individual circular Rydberg atoms, which are highly excited atoms with a correspondingly very large dipole momentum, interacting with single photons in a ultra-high quality factor microwave cavity. This pioneering experiment represents a 25-year-long research effort and has established most of the concepts and ideas of the field of Cavity Quantum Electrodynamics (Cavity QED), which describes the coherent interaction of single atoms with single photons trapped in one mode of an electromagnetic cavity. This experiment is widely recognized as a constant source of inspiration for quantum physics as a whole, and this is particularly true for the field of superconducting qubits. Cavity QED is an ideal system to develop a deeper understanding and intuition of quantum mechanics, and this was my main motivation as a PhD student. My contribution consisted in demonstrating the entanglement of two Rydberg atoms by a controlled collision inside the cavity [1], and in performing the first quantum state tomography of a field in a cavity by measuring its Wigner function, a method that I applied to the single-photon Fock state [2]. In this manuscript I will describe this last experiment.

After this PhD in atomic physics, I opted for a postdoc in mesoscopic physics, in order to broaden my views and perspective of quantum physics and apply them to solid-state systems. In Delft, in the Quantum Transport Group under the direction of Hans Mooij, I discovered the field of superconducting quantum circuits and learned its techniques. The group main research topic was the flux-qubit circuit. I teamed up with Irinel Chiorescu, postdoc in the group at that time, who had observed the coherent dynamics of a flux-qubit just before my arrival. In a new sample, we observed and explained the strong coupling of the flux-qubit to an on-chip LC oscillator which was part of the qubit detection circuit [3]. This strong coupling was manifested by the appearance of sideband transitions in which both the qubit and resonator quantum state were changed, in perfect analogy with ion-trap experiments performed by D. Wineland group at NIST in particular. This work was published back-to-back with the ground-breaking experiment performed at the same time at Yale by A. Wallraff and R. Schoelkopf [4], also reporting the strong coupling of a qubit to a microwave photon in a complementary setup, and both works attracted some attention [5] since they opened the perspective of applying the most advanced concepts and tools of atomic physics to solid-state systems. These promises have been fully met with the impressive development of circuit QED as a new independent research field. Another contribution during my postdoc was to identify, investigate, and suppress, various mechanisms by which the flux-qubit was losing its quantum coherence, which allowed us to reach record coherence times (at that time) of several

microseconds [6]. In the manuscript I will give a brief account of these two results.

1.3 Circuit QED with Superconducting Qubits

In the second part of this manuscript I will describe research performed since I joined the Quantronics Group in CEA Saclay, after my postdoc, as permanent researcher to further develop research on superconducting qubits, teaming up with Denis Vion and Daniel Esteve. The group was previously doing research on the Quantronium circuit design, using DC electrical transport measurements to readout the qubit state. Upon my arrival, it became clear that microwave measurements at a few-photon level were extremely promising for quantum and more generally mesoscopic physics. I thus started a new activity on circuit QED with transmon qubits driven and measured via superconducting coplanar resonators, inspired by the work performed at Yale in R. Schoelkopf group. In this way I learned how to perform state-of-the-art ultra-low-noise microwave measurements.

Circuit QED research in the Quantronics group took two parallel paths. On one side we developed a research activity on the theme of weak continuous measurements, based on ideas by A. Korotkov, which was mainly carried out by Agustin Palacios-Laloy during his PhD (of whom I was the main supervisor). This activity culminated with the test and violation of the "Leggett-Garg inequality" which brought further proof of the non-classical nature of superconducting qubits [7]. These experiments are described in A. Palacios-Laloy PhD thesis [8] and will be described in this manuscript.

I will not describe here the other research path followed in our group, in the more applied goal of making progress towards a scalable superconducting quantum processor architecture based on transmon qubits. Compared to similar research projects in other groups, we developed a qubit readout method based on the bistability of a non-linear resonator to which the qubit is coupled [9], following previous work in particular with flux-qubits [10], which yielded the first high-fidelity single-shot transmon qubit readout in circuit QED [11] (these experiments were mainly carried out by postdoc François Mallet, whom I was co-supervisor). This readout method was used by A. Dewes during his thesis (whom I co-supervised) to demonstrate a two-qubit gate and the quantum speed-up of a simple two-qubit algorithm compared to its classical counterpart; and it is at present used by V. Schmitt (PhD student) to develop a 4-qubit processor. In the process of understanding the readout of the transmon qubit by the nonlinear resonator we were led (together with postdoc Florian Ong whom I co-supervised) to investigate on a more fundamental level the strong coupling of this two-level system and of the non-linear resonator, a new playground for quantum optics that could be nicknamed nonlinear circuit QED [12, 13].

1.4 Hybrid Quantum Circuits

Since 2009 I have somewhat shifted interest towards a new research activity which aims at coupling spins in crystals to superconducting quantum circuits. The general motivation is that spins in crystals can have extremely long coherence times (up to seconds for electronic spins, up to hours for nuclear spins), with frequencies in the

microwave domain matching those of superconducting circuits. It is thus appealing to imagine novel types of quantum devices combining coherently spins and circuits, which would benefit both of the long spin coherence times, and of the flexibility and strong coupling to electromagnetic fields of electrical circuits. At present this spin-based hybrid project occupies most of my research activity, with Denis Vion supervising the work on transmon-based circuit QED.

Our first project in this direction uses large ensembles of spins ($\approx 10^{11}$) to store the state of superconducting qubits. The project was started in 2009 together with Y. Kubo, a Japanese postdoc whom I supervised on this topic. We first brought a spectroscopic evidence for the strong coupling of an ensemble of 10^{12} NV centers to a resonator by measuring a normal mode splitting between the two systems [14]. This experiment attracted some attention as it was considered the first result of a new field of spin-based hybrid quantum circuits. Since then, we have brought the first proof-of-principle of spin-based quantum memory for a superconducting qubit [15], and we have demonstrated the potential of hybrid quantum circuits for high-sensitivity electron-spin resonance detection [16]. More recently, we have been trying to use spin-echo techniques to extend the quantum memory storage time to longer values, with an initial goal of 100μs. This is the project of a PhD student, Cécile Grezes, of whom I am the main supervisor since her start in 2011. An overview of this research on spin ensemble quantum memory will be given in this manuscript.

In parallel, I have launched a second project since 2012, with postdoc Michael Stern, and PhD student Audrey Bienfait (of whom I am main supervisor), which I will not describe here by lack of space. Its goal is to couple individual spins to superconducting resonators and qubits. If successful, this would allow to entangle distant spins using microwave photons as mediators for the interaction. Detecting single spins with microwave signals would also have an impact on the field of magnetic resonance, since it would represent a gain in sensitivity by 10 orders of magnitude compared to commercial spectrometers. The challenge is to increase the coupling constant of the unique spin to the superconducting circuit.

Chapter 2

From Cavity QED to Circuit QED

This chapter relates work performed during my PhD thesis in the Laboratoire Kastler-Brossel at ENS Paris on Rydberg atoms strongly coupled to a microwave cavity, and during my postdoc in the Quantum Transport group at Delft Technical University in the Netherlands with flux-qubits coupled to on-chip resonators. Playing with Rydberg atoms and microwave photons during my PhD thesis in S. Haroche group, under the guidance of Jean-Michel Raimond and Michel Brune in particular and together with PhD students G. Nogues, A. Rauschenbeutel, and S. Osnaghi, was a unique opportunity to acquire an intuition of how the most fundamental concepts of quantum physics apply to systems of coupled individual particles. One of the results obtained, which I will present in the manuscript, is the first full quantum tomography of a one-photon Fock state of the microwave field, revealing its strong non-classical character by negative values of its Wigner function. This intuition of coupled quantum systems acquired during my thesis proved very useful during my postdoc in Delft when, quite unexpectedly, we found out that our flux-qubit sample was in strong coupling with a stray harmonic oscillator in its close environment. With H. Mooij, K. Harmans, and I. Chiorescu, we were thus led to apply the cavity QED concepts and models to superconducting circuits, which eventually developed further into the new field of Circuit QED.

2.1 Cavity Quantum Electrodynamics with Rydberg atoms

One of the main motivations of the Cavity QED group at ENS is to achieve the highest degree of control over the state of the electromagnetic field, using individual atoms both to manipulate its quantum state and to reveal its properties. In this goal, the group has developed over many years a setup whose core elements are shown in Fig. 2.1: individual Rydberg atoms cross and interact with the electromagnetic field in a high-quality factor microwave cavity. During my thesis I have in particular demonstrated how these Rydberg atoms can be used to bring the most complete characterization of the field possible, by measuring its so-called Wigner function. I have applied this method to a strongly non-classical state of the field, also prepared in the cavity by Rydberg atoms : the one-photon Fock state. I will first give an overview of the key concepts in cavity QED.

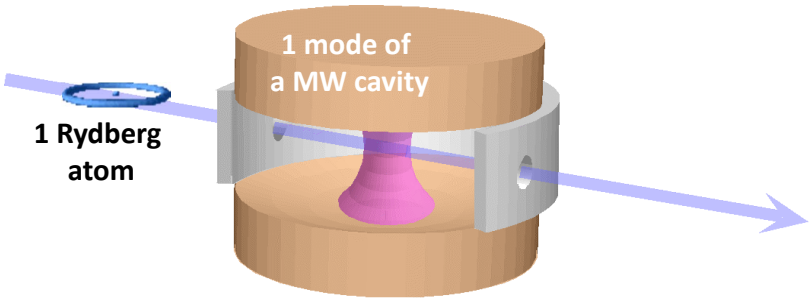

Figure 2.1: Cavity QED Principle. Individual Rydberg atoms cross and interact with the electromagnetic field stored in a high-quality factor mode of a Fabry-Pérot superconducting microwave cavity at 51.1 *GHz. The cavity is surrounded by a metallic ring to increase its quality factor.*

2.1.1 The atom-field system

The cavity QED experiments need to be performed in the strong coupling regime, where the atom-field coupling strength is larger than the decay rate of both the field and the atom. The system Hamiltonian $H = H_{at} + H_c + H_{int}$ is the sum of the atom Hamiltonian H_{at}, of the field Hamiltonian H_c and the interaction Hamiltonian H_{int}. The atom is described as a two-level system with ground state $|g\rangle$ and excited state $|e\rangle$, and transition frequency ω_0 so that

$$H_{at} = -\frac{\hbar\omega_0}{2}\sigma_z, \tag{2.1}$$

σ_z being the Pauli operator. The cavity Hamiltonian is

$$H_c = \hbar\omega_c a^\dagger a, \tag{2.2}$$

with ω_c the cavity frequency and a (resp. $a^\dagger$) the field annihilation (resp. creation) operator. The atom-field interaction is of the electric dipolar type

$$H_{int} = -\overrightarrow{d} \cdot \overrightarrow{E}. \tag{2.3}$$

Restricting the dipole operator to the two atomic levels $\overrightarrow{d} = \langle g|\overrightarrow{d}|e\rangle(\sigma_+ + \sigma_-)$ (for atoms with purely transverse dipole such as circular Rydberg atoms), and rewriting the electric field operator $\overrightarrow{E} = \overrightarrow{\delta E_0}(a + a^\dagger)$ we get

$$H_{int} = \hbar g(\sigma_- + \sigma_+)(a + a^\dagger) \tag{2.4}$$

where

$$g = -\frac{\langle g|\overrightarrow{d}|e\rangle \cdot \overrightarrow{\delta E_0}}{\hbar} \tag{2.5}$$

is the so-called atom-field coupling constant. Going one step further we apply the Rotating Wave Approximation in this interaction Hamiltonian, which consists in neglecting the non-energy-conserving terms $\sigma_+ a^\dagger$ and $\sigma_- a$. In the end, in the rotating frame at ω_c the atom-field is then described by the Hamiltonian

$$H/\hbar = \frac{\delta}{2}\sigma_z + g(\sigma_- a^\dagger + a\sigma_+), \tag{2.6}$$

with $\delta = \omega_0 - \omega_c$ the atom-field detuning. This is the so-called Jaynes-Cummings model which is the theoretical framework of cavity quantum electrodynamics. More generally, this model describes the linear coupling of a two-level system with a harmonic oscillator, which will appear several times in this manuscript.

2.1.2 Jaynes-Cummings Hamiltonian

The physics of the Jaynes-Cummings model is described in several references [17]. Without giving the detail of the calculations, we now describe the two different regimes of the Jaynes-Cummings model that are relevant for this work : the resonant regime $\delta = 0$, and the dispersive regime $|\delta| \gg g$.

The resonant regime : vacuum Rabi oscillations

When the atom and field are in resonance ($\delta = 0$), they can exchange energy. If we prepare the atom in the excited state while the field is in vacuum, the Jaynes-Cummings Hamiltonian predicts that the atom-field system evolves as

$$|\psi(t)\rangle = \cos gt|e,0\rangle + i \sin gt|g,1\rangle \tag{2.7}$$

implying that the atom excited state probability varies as $P(e) = (\cos 2gt + 1)/2$. This describes the periodic emission and re-absorption of a single microwave photon with a period π/g, a phenomenon called vacuum Rabi oscillations. Vacuum Rabi oscillations are a precious tool for the generation and control of non-classical states. First, stopping the atom-cavity interaction at time $\tau_\pi = \pi/(2g)$ prepares the cavity in the 1-photon Fock state $|1\rangle$ (this is called a "quantum π pulse"). Also useful is the quantum $\pi/2$ pulse where the atom-field interaction is stopped at $\tau_{\pi/2} = \pi/(4g)$, preparing the atom-cavity system in the maximally entangled state $(|e,0\rangle + i|g,1\rangle)/\sqrt{2}$.

The dispersive regime : QND measurements

The opposite regime $|\delta| \gg g$ where the atom is largely detuned from the field is the so-called dispersive regime. Because of the detuning, atom and field can no longer exchange energy, and their interaction is described by energy shifts. The Jaynes-Cummings interaction Hamiltonian can then be approximated by the dispersive Hamiltonian

$$H_{disp}/\hbar = \frac{\delta}{2}\sigma_z + \chi a^\dagger a \sigma_z. \tag{2.8}$$

with $\chi = g^2/\delta$ the dispersive coupling constant. This Hamiltonian has the very interesting property to commute both with H_{at} and with H_c, which implies that the atom-cavity dispersive coupling can be used for Quantum Non-Destructive measurements of both the atomic state and the photon number distribution. More precisely, the dispersive Hamiltonian can be interpreted by the fact that the cavity frequency $\omega_c + \chi\sigma_z$ now slightly depends on the qubit state, which is used for instance in circuit QED for qubit measurements, as discussed in the next chapter. Recasting the terms of the same dispersive Hamiltonian differently, one also sees that the qubit frequency $\omega_0 - 2\chi n$ now depends on the photon number n in the cavity, a phenomenon called ac-Stark shift. This means that the phase acquired by a

qubit state superposition will bring some information about the photon number distribution in the cavity. This is the basis for the Wigner function measurement, as well as for experiments performed in the ENS group after my thesis, reporting the observation of quantum jumps of the field in the cavity [18].

2.1.3 Experimental setup

Cavity QED experiments are performed both in the optical and the microwave domains, with very different techniques. Microwave circuit QED requires atomic transitions at microwave frequencies, with a dipole moment as large as possible, which is achieved with circular Rydberg states, as well as a very high-quality factor cavity, obtained with a superconducting Fabry-Perot resonator.

Rydberg atoms

Rydberg states are highly excited atomic states (large principal quantum number n), which are characterized by a strong dipole moment. The experiment worked with special Rydberg states called "circular Rydberg states" in which also the angular momentum of the atom is maximal ($m = l = n-1$). We used as ground state $|g\rangle$ the circular Rydberg state $|n = 50, l = m = 49\rangle$ of ^{85}Rb, and as excited state the circular Rydberg state $|n = 51, l = m = 50\rangle$, with an atomic frequency $\omega_0/2\pi = 51.099\,\mathrm{GHz}$. The size of the atomic orbital in these states is of order 100 nm, which helps to understand that the dipole moment between $|g\rangle$ and $|e\rangle$ is 1700 times larger than the hydrogen atom. From the state $|e\rangle$ the atom can only relax into state $|g\rangle$, and this occurs by spontaneous emission in $\approx 30\,\mathrm{ms}$.

Exciting a Rubidium atom from its ground state into $|g\rangle$ is a difficult task, achieved in the experiment by a combination of 3 lasers, radiofrequency and microwave excitations. Note that Rydberg atoms are sensitive to radiation at their resonance frequency around 50 GHz and therefore need to be in a cryogenic environment to remain in a pure quantum state.

The superconducting cavity

The cavity consists in two superconducting mirrors facing each other, in a Fabry-Pérot configuration, machined out of niobium. The mode of interest is close to the atomic frequency, at 51.1 GHz. At a temperature of 1 K, its quality factor was measured to be $Q = 3 \cdot 10^8$, corresponding to a photon lifetime $\kappa^{-1} = Q/\omega_c = 1\,\mathrm{ms}$. To reach this large value, it was necessary to add a metallic ring around the cavity, whose goal is to "recycle" the microwave photons scattered by the mirror imperfections, and thus to increase Q (as can be seen in Figs. 2.1 and 2.2). It is essential that the field in the cavity is in its ground state, which implies that the mean photon number in the cavity due to thermal excitations should be much smaller than 1. The experiments are performed at 1.5 K yielding ≈ 0.1 photon at 51 GHz. Calibration experiments show that the atoms crossing the cavity reach a maximum coupling constant $g/2\pi = 25\,\mathrm{kHz}$, which places the setup largely in the strong coupling regime.

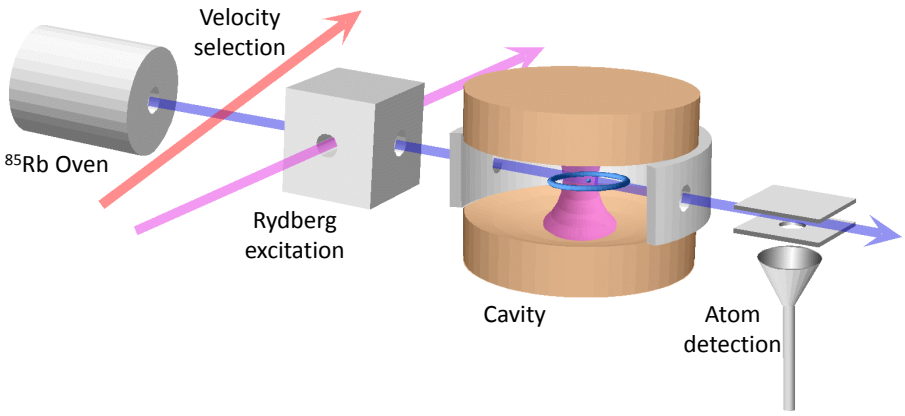

Figure 2.2: Cavity QED Setup. The Rubidium atoms effuse out of an oven, cross a zone where their velocity are selected by optical pumping, and are then excited into the Rydberg state. After crossing the cavity they are detected by field-ionization.

The experimental setup

An overall schematics of the experimental setup is shown in Fig. 2.2. Rubidium atoms are effusing out of an oven, then crossing the whole setup. After a laser repumping scheme that allows to select only atoms with a chosen velocity, the atoms enter the cryostat. They are first transferred into the circular Rydberg state $n = 50$, then enter the microwave cavity. In the cavity, they can be excited by classical microwave pulses (not shown in Fig. 2.2), or interact with the quantum field stored in the cavity. A DC voltage is applied accross the cavity mirrors, in order to tune the atom frequency by Stark effect in a time-resolved manner. This allows to control precisely the atom-field interaction time.

2.1.4 Measurement of the Wigner function of a one-photon Fock state in the cavity

I will now present the results obtained during my PhD on the measurement of the Wigner function of a one-photon Fock state in the cavity [2].

The Wigner function

The Wigner function of an electromagnetic field $W(\alpha)$ is a quasi-distribution of probability in phase space that contains all the information about the statistical properties of this field [17]. It is thus equivalent to the field complete density matrix ρ. Several equivalent definitions exist, but for our purpose the most useful one is

$$W(\alpha) = 2Tr[D(-\alpha)\rho D(\alpha)P], \tag{2.9}$$

with $D(\alpha) = e^{\alpha a^\dagger - \alpha^* a}$ the displacement operator, and $P = e^{i\pi a^\dagger a}$ the parity operator. The Wigner function is thus the average value of the photon number parity in the cavity field displaced by $-\alpha$. With this definition the Wigner function is normalized such that $\int W(\alpha) d^2\alpha = \pi$ for all field states.

The Wigner function has a simple physical interpretation, since integrated along one quadrature I of the field it directly gives the probability distribution of the orthogonal quadrature Q (and hence the square of its wavefunction if the field is in a

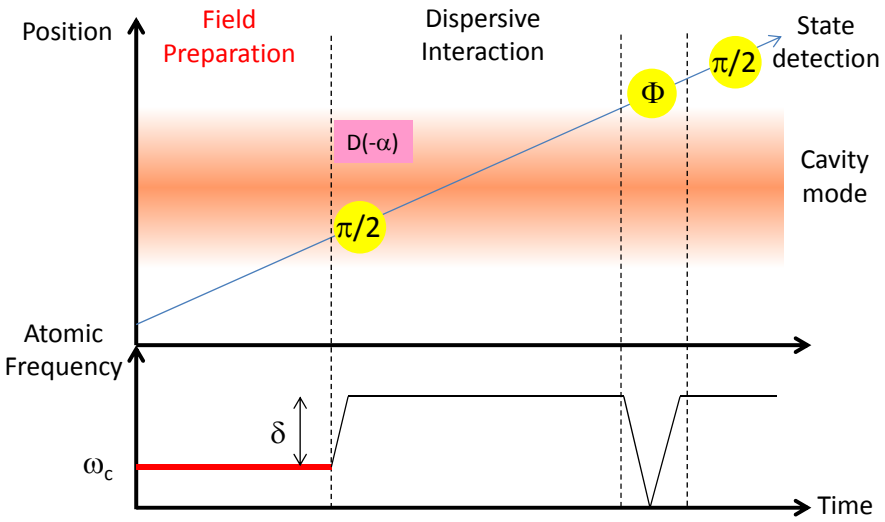

Figure 2.3: Protocol for Wigner function measurement. A single atom is used first to prepare the field in the state to be measured, then for the Wigner function measurement scheme. After the state preparation step, the atom is detuned, a $\pi/2$ pulse is applied while the cavity state is displaced by $-\alpha$, and a dispersive cavity-atom interaction takes place with a phase shift of π per photon. After the interaction, the atomic dipole is phase-shifted by Φ by Stark-tuning, then the atom undergoes a final $\pi/2$ pulse before detection.

pure quantum state). One interesting feature is that it is positive for all classical or quasi-classical field states (thermal state, coherent state, or even squeezed states), but takes negative values for non-classical states such as Fock states or Schrödinger-cat states. First measurements of the Wigner function of an electromagnetic field were achieved in the optical domain [19, 20] by homodyne detection. The results obtained during my PhD are the first Wigner function measurements in the microwave domain.

Principle of the measurement

According to Eq. 2.9, measuring W can be achieved in Cavity QED by first preparing the cavity field in an interesting state ρ, displacing it by $-\alpha$ (which is done conveniently by switching on a classical source with adequate amplitude for a chosen time), and finally measuring $\langle P \rangle$. In our experiment we realize this parity measurement based on a proposal by Lutterbach and Davidovich [21]. It relies on the dispersive atom-field interaction of cavity QED, in the regime where one photon is enough to impart a phase shift of π to an incoming atomic dipole, which according to Eq. 2.7 corresponds to an atom-field interaction time $\tau = \pi/(2\chi) = \pi\delta/(2g^2)$.

The measurement of $W(\alpha)$ is achieved by combining this "π per photon" phase shift with Ramsey interferometry, as described in Fig. 2.3. Indeed, if an atom is prepared in $(|e\rangle + |g\rangle)/\sqrt{2}$ by a first classical $\pi/2$ pulse before interacting with the displaced cavity field at detuning δ for a duration of τ, it exits the cavity in state $(|e\rangle + (-1)^n|g\rangle)/\sqrt{2}$, n being the photon number in the cavity. After a second $\pi/2$ pulse with a varying phase Φ, the probability $p_e(\Phi, \alpha)$ of finding the atom in $|e\rangle$ if the cavity contains n photons is $p_e(\Phi, \alpha) = (1 + \cos\Phi)/2$ if n is even and $(1 - \cos\Phi)/2$ if n is odd. For an arbitrary photon number distribution, we get that

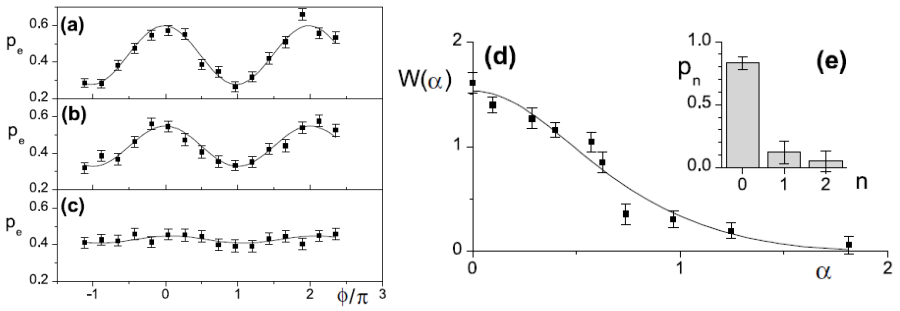

Figure 2.4: Wigner function of a thermal field. (a,b,c) Ramsey fringes obtained with the field prepared in a thermal state, for $\alpha = 0, 0.57$, and 1.25 respectively. (d) Corresponding measured Wigner function (full squares) and fit to a Gaussian (solid line), yielding a mean thermal photon number $n_{th} = 0.2$. (inset) Corresponding photon number occupation probabilities. (Extracted from [2]).

$p_e(\Phi, \alpha) = (1 + \langle P \rangle \cos \Phi)/2$. In the end, the Wigner function $W(\alpha)$ is thus directly linked to the fringe contrast $c(\alpha)$ by the relation

$$W(\alpha) = 2c(\alpha) = 2[p_e(0, \alpha) - p - e(\pi, \alpha)]. \tag{2.10}$$

Wigner function of the vacuum

To test the measurement principle on a simple field state, we have performed the measurement on a small thermal field present in the cavity, caused by insufficient attenuation in the input waveguides of the setup. The Wigner function of such a state is expected to be a Gaussian with a standard-deviation $\sqrt{1 + 2n_{th}}$, n_{th} being the average thermal photon number. A schematics of the experimental sequence is provided in Fig. 2.3.

The results are shown in Fig. 2.4. Ramsey fringes are shown for various values of the displacement field α, with α being calibrated prealably by measuring the ac-Stark shift of an atom in the same field [2]. Note that since the initial state, being a thermal state, has no phase, the Wigner functions that we measure are by construction rotationally-invariant and the phase of α is irrelevant. In the following we will therefore assume α to be real. In Fig. 2.4 one notices that the phase of the Ramsey fringes does not depend on α; only their contrast is reduced, which shows that the condition of π phase shift per photon is properly satisfied. Computing $W(\alpha)$ from the Ramsey fringe measurements using Eq. 2.10 yields a Wigner function which is not properly normalized due to the finite contrast of the interferometer caused by mostly by stray electric and magnetic fields. To turn the Ramsey fringe measurements into a physically meaningful Wigner function, the data are multiplied by a normalizing factor ensuring that $\int W(\alpha) d^2\alpha = \pi$. This procedure assumes that the interferometer contrast is independent on α, which is reasonable given that the factors limiting the contrast can be quantitatively identified [22]. The measurements analyzed in this way are in good agreement with the expected Wigner function of a thermal field with a photon number $n_{th} = 0.2$.

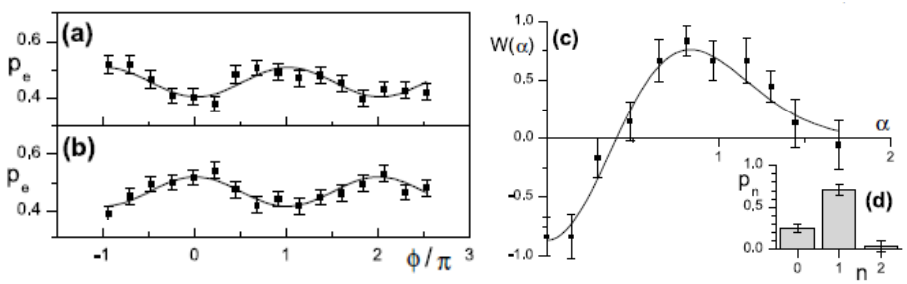

Figure 2.5: Wigner function of a one-photon Fock state.(a,b) Ramsey fringes obtained with the field prepared in a one-photon Fock state (by preparing the atom in initial state $|e\rangle$ and keeping it resonant with the cavity for a quantum π pulse), for $\alpha = 0$ and 0.81. Note that the fringes have been π phase shifted, corresponding to a change of sign of $W(\alpha)$. (c) Corresponding measured Wigner function (full squares) and fit to a statistical mixture of $|0\rangle$, $|1\rangle$ and $|2\rangle$ states (solid line), showing the expected negative value around $\alpha = 0$. (inset) Corresponding photon number occupation probabilities. (Extracted from [2]).

Wigner function of a single-photon Fock state

After this calibration experiment, we now turn to a more interesting situation where the cavity is prepared in a 1-photon Fock state. As explained in 2.1.2, this is achieved using the vacuum Rabi oscillations of an atom initially prepared in $|e\rangle$ and interacting with the cavity vacuum field for a duration τ_π. In order to minimize the delay between the cavity field state preparation and its measurement which is crucial for its fidelity, we decided to use the same atom to generate the photon and to probe it. The atom thus enters the cavity when prepared in $|e\rangle$, is kept in resonance with the mode for τ_π, and is then detuned by the electric field across the mirrors to the detuning δ required to satisfy the π-per photon condition during the remaining atom-field interaction time (see again Fig. 2.3).

The results are shown in Fig. 2.5, with two Ramsey fringes measured respectively at $\alpha = 0$ and $\alpha = 0.81$. While the phase of the $\alpha = 0.81$ fringes is identical to the one measured in the vacuum case, the phase of the $\alpha = 0$ fringes is π-phase shifted, a striking indication that $c(0)$ and therefore $W(0)$ have become negative as expected for $|1\rangle$. As in the previous pragraph $W(\alpha)$ is determined by multiplying $c(\alpha)$ by a factor ensuring that the Wigner function is properly normalized. The factor is larger than in the vacuum measurement because the interferometer contrast is further reduced by the imperfections of the π pulse. The measured Wigner function corresponds to a density matrix with a one-photon occupation probability of 0.71, which is well explained by the known experimental imperfections.

Since this first measurement of the Wigner function of a non-classical field state in a cavity [2], many exciting developments have taken place during the last 5 years, with Wigner functions of higher-order Fock states and Schroedinger-cat states reported both in cavity QED [23] and in circuit QED [24].

2.2 Flux-qubit coupled to a LC oscillator

My postdoc at TU Delft took place in the field of superconducting qubits that I discovered on that occasion. Superconducting qubits are artificial atoms made with electrical circuits with capacitors, inductors, and Josephson junctions as their

building blocks. My motivation was to experience quantum effects in a solid-state context, which I imagined to be more "dirty" than atomic physics and therefore possibly to offer more potential to discover new effects. I was very far from realizing that my experience in cavity QED would apply itself so literally, as explained in the following.

2.2.1 Historical context

It is useful to say a few words about the historical context in which my postdoc took place, especially considering the rapid evolution of the field since then.

The idea that superconducting circuits could be used to build artificial two-level systems useful for quantum physics and quantum information dates back to $1995 - 1996$. If several signatures of quantum behavior were observed in various circuits in the years $1997 - 1999$, the key pioneering experiment marking the birth of the field is the obervation of the coherent dynamics of a Cooper-pair box (one of the major qubit designs) by Y. Nakamura, Y. Pashkin and J.-S. Tsai at NEC in 1999 [25]. The very fact that macroscopic, man-made electrical circuits could display the same quantum-mechanical behavior as a simple two-level atom was perceived as a major surprise by many physicists, even though the coherence time was only of a few nanoseconds in this experiment.

At approximately the same time, Hans Mooij and coworkers [26] proposed a circuit design called the flux-qubit (FQ) which consists of a superconducting loop interrupted with 3 Josephson junctions, described in more detail below. The interest of the flux-qubit design is its insensitivity to charge-noise, which was thought to limit the coherence times in Nakamura's experiment with the Cooper-pair box (together with its coupling to the measurement circuit). Since the 1999 proposal, the basic working principle of the FQ was experimentally demonstrated in Delft in 2000 with spectroscopic measurements [27].

In 2001 the coherent dynamics of a Cooper-pair box was again observed in Saclay [28]. But compared to the NEC experiment, several changes were made which brought a gain of nearly 3 orders of magnitude in coherence time, up to 500 ns. First, the Cooper-pair box parameters were chosen to make it less sensitive to charge noise. Then, a novel read-out circuit was designed to measure the qubit state in a single shot, based on the qubit-state dependent switching of a large Josephson junction to the voltage state. This circuit, nicknamed the Quantronium, allowed to minimize the back-action of the read-out circuitry during operation of the qubit, while being able to measure the qubit state quickly enough afterwards by pulsing the current through the read-out junction [28]. One essential outcome of the experiment was the study of the Quantronium coherence time (both with Ramsey fringes and spin-echo) as a function of its bias point, and the evidence that coherence is maximized at the so-called optimal points where the qubit frequency becomes insensitive to the fluctuations of some control parameter (either the gate charge or the bias flux in the case of the Quantronium).

Inspired by the Quantronium experiment, the Delft team (in particular I. Chiorescu and Y. Nakamura, by then a visitor in Delft) succeeded in 2002, just before my arrival, to observe the coherent dynamics of a flux-qubit [29], with a read-out circuit consisting of a switching SQUID instead of a switching junction. The coherence time measured in that experiment was relatively short compared to the Quantro-

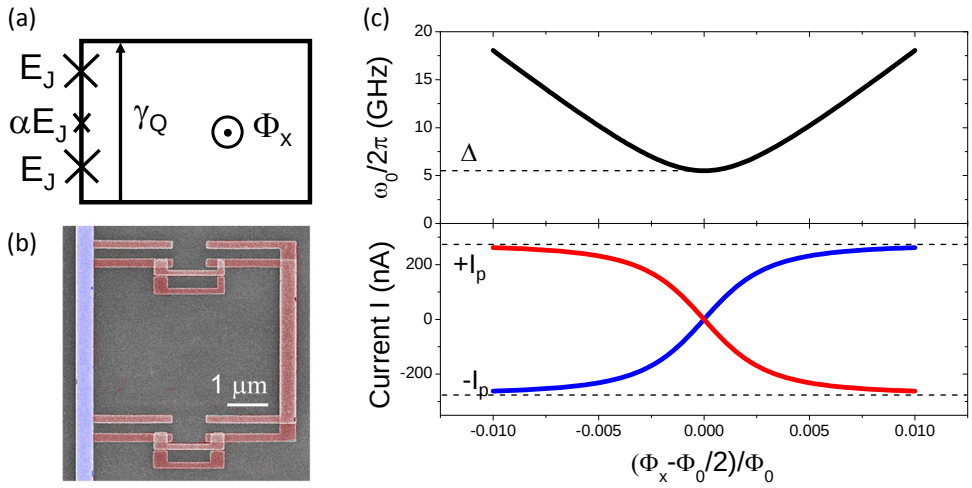

Figure 2.6: Flux-qubit principle. (a) The flux-qubit is a superconducting loop that includes three Josephson junctions, one of them being smaller than the two others by a factor $\alpha \approx 0.5 - 0.7$. *The Josephson energy of the large junctions is* E_J. *The loop is biased by an external magnetic flux* Φ_x *which imposes a phase bias across the three junctions* $\gamma_Q = 2\pi\Phi_x/\Phi_0$. *(b) Scanning Electron Micrograph of a typical flux-qubit sample (here with* 4 *junctions and not* 3*), made of Aluminum electrodes and Aluminum Oxide Josephson junctions. (c) (top) Transition frequency* ω_0 *between the flux-qubit energy levels* $|0\rangle$ *and* $|1\rangle$. *At* $\Phi_x = \Phi_0/2$ *one has* $\omega_0 = \Delta$ *and the qubit frequency is first-order insensitive to* Φ_x *(optimal point). (bottom) Persistent current* $\langle\hat{I}\rangle$ *for states* $|0\rangle$ *(blue solid line) and* $|1\rangle$ *(red solid line).*

nium results, around $20 - 30$ ns. As a postdoc I was given the task to study in detail the coherence times of the flux-qubit in order to identify the limiting factors. In particular it seemed interesting to measure the flux-qubit coherence times at its optimal biasing point for flux-noise (see below), to confirm the Saclay results about increased coherence. This had not been possible in the initial experiment [29].

During this study of decoherence, I was quickly led to investigate the coupled dynamics of the flux-qubit and its measurement circuit. It turned out that to understand our data it was necessary to model the two systems quantum-mechanically, with a Hamiltonian describing the strong-coupling of the qubit two-level system with a harmonic oscillator. Exactly at the same time, R. Schoelkopf and A. Wallraff at Yale observed the first vacuum Rabi splitting between a coplanar resonator and a Cooper-pair box, a major breakthrough for the field of superconducting circuits. These two experiments made it clear that the appropriate conceptual framework to describe superconducting circuits was the same as the one needed to describe the interaction between Rydberg atoms and the microwave field, namely quantum electrodynamics and the Jaynes-Cummings Hamiltonian. This was a contribution towards the development of circuit quantum electrodynamics as explained in the next chapter.

2.2.2 System description

The flux-qubit

The flux-qubit consists of a superconducting loop interrupted with 3 (or 4 in more modern designs) Josephson junctions, one of them being smaller than the others by a factor $\alpha \approx 0.5 - 0.7$ (see Fig. 2.6). When biased by an external magnetic flux Φ_x close to $\Phi_0/2$ ($\Phi_0 = h/2e$ being the superconducting flux-quantum), which imposes a phase drop across the 3 junctions $\gamma_Q = \Phi_x/(2\pi\Phi_0) \approx \pi$, two states of the circuit $|\circlearrowright\rangle$ and $|\circlearrowleft\rangle$ corresponding to a persistent current I_p flowing clockwise or counter-clockwise in the loop are quasi-degenerate in energy. Because of charging effects, there exists a quantum tunneling rate Δ between these two states. As a result their degeneracy is lifted and the resulting energy eigenstates $|0\rangle$ and $|1\rangle$ are coherent superpositions of $|\circlearrowright\rangle$ and $|\circlearrowleft\rangle$, with a transition frequency $\omega_0(\gamma_Q)/2\pi = \sqrt{\Delta^2 + \epsilon^2}$, $\epsilon = I_p\Phi_0(\gamma_Q/\pi - 1)/h$ being the detuning between the two classical states $|\circlearrowright\rangle$ and $|\circlearrowleft\rangle$ (see Fig. 2.6).

Here we will write the flux-qubit Hamiltonian in the energy basis so that

$$H_{FQ} = -\hbar\omega_0\sigma_z/2, \tag{2.11}$$

with $\sigma_{z,x}$ the usual Pauli matrices. Note that in the literature the flux-qubit Hamiltonian is often written in other bases : either the persistent-current basis $|\circlearrowright\rangle, |\circlearrowleft\rangle$ yielding $H_{FQ2} = -\frac{\hbar\omega_0}{2}(\cos\theta\sigma_z + \sin\theta\sigma_x)$, or in the basis of the energy eigenstates at $\gamma_Q = \pi$ (so-called transverse basis) $|0\rangle = (|\circlearrowright\rangle + |\circlearrowleft\rangle)/\sqrt{2}$ and $|1\rangle = (|\circlearrowright\rangle - |\circlearrowleft\rangle)/\sqrt{2}$, in which case $H_{FQ3} = -\frac{\hbar\omega_0}{2}(\cos\theta\sigma_x + \sin\theta\sigma_z)$. In these expressions $\theta(\gamma_Q)$ is a mixing angle defined by $\sin\theta = \Delta/\omega_0$ and $\cos\theta = \epsilon(\gamma_Q)/\omega_0$ that will be encountered in several formulas below. In this manuscript we will only use the energy basis (that is H_{FQ}), yielding sometimes different expressions from the literature.

As seen in Fig. 2.6b, we note that $d\omega_0/d\gamma_Q = 0$ for $\gamma_Q = \pi$ (which corresponds to $\Phi_x = \Phi_0/2$). This is thus an optimal point with respect to magnetic flux noise. We also show in Fig 2.6b the average circulating current in each of the two states which are opposite, making possible to discriminate between the two states during qubit readout.

Principle of the flux-qubit readout

This circulating current is the basis for the flux-qubit readout principle in our experiments as depicted in Fig. 2.7. Indeed, the flux-qubit is coupled with a mutual inductance M to the loop of a DC-SQUID (see Fig. 2.7a). The different circulating currents generate a flux $\Phi_{Sq}^{(i)}$ $(i = 0, 1)$ in the SQUID, resulting in different critical currents $I_C^{(i)}$ with for instance $I_C^{(1)} < I_C^{(0)}$. At the end of the experimental sequence, the SQUID bias current I_b is suddenly ramped from its initial value to a value chosen between $I_C^{(1)}$ and $I_C^{(0)}$ so that the SQUID switches to the voltage state if the qubit is in $|1\rangle$ and not if it is in $|0\rangle$ (see Fig. 2.7b), generating a voltage pulse easily detected at room-temperature. In other words the SQUID is used as a sample-and-hold detector amplifying the small difference between the two states. Ideally the SQUID switching probability P_{sw} should thus be equal to the probability to find the qubit in $|1\rangle$ P_1. Measurements are shown in Fig. 2.7c, with the SQUID switching probability plotted as a function of I_b for the qubit prepared in states $|0\rangle$ and $|1\rangle$. In reality

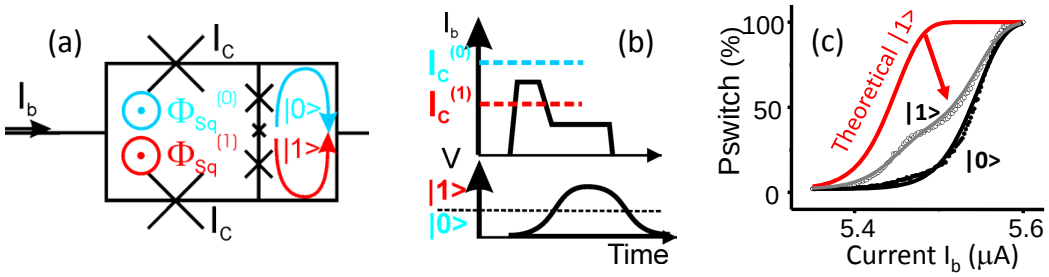

Figure 2.7: Flux-qubit readout. (a) The qubit is inductively coupled to a DC SQUID with junctions having a critical current I_C, and biased by a current I_b. The flux seen by the SQUID becomes qubit-state dependent. (b) Readout pulse. The SQUID bias current is ramped at a value such that the SQUID switches if the qubit is in $|1\rangle$ and not if it is in $|0\rangle$ yielding a measurable voltage pulse. (c) Typical measured SQUID switching probability as a function of bias current for the qubit in state $|0\rangle$ (black dots) and $|1\rangle$ (open dots). An erf function is used to fit the curve with the qubit in $|0\rangle$ (black solid line); the red solid line shows the expected curve for qubit in $|1\rangle$. The grey line is a weighted sum of the two curves, showing that the qubit has relaxed from $|1\rangle$ to $|0\rangle$ at the time of the measurement.

because of qubit energy relaxation during the readout pulse, one can only say that the switching probability P_{sw} is a linear function of P_1 (see Fig. 2.7c).

Qubit - plasma mode coupling

In the purpose of narrowing the SQUID switching events histogram, which is essential for a high fidelity qubit readout, the SQUID is shunted in our circuit by an on-chip capacitor C_{sh}, to which it is connected by superconducting lines having an inductance L, as described in Fig. 2.8. Since the SQUID itself behaves as a Josephson inductance $L_J(\Phi_{Sq})$, this readout circuit behaves as a LC resonator with inductance $L + L_J(\Phi_{Sq})$ and capacitance C_{sh}. This resonator is traditionally called "the plasma mode" and has a frequency $\omega_p = 1/\sqrt{(L + L_J(\Phi_{Sq}))C_{sh}}$. Its Hamiltonian is $H_p = \hbar\omega_p a^\dagger a$, with a and $a^\dagger$ the usual annihilation and creation operators for single quanta in this electromagnetic resonator. They are related to the plasma mode current operator $i_p = \delta i_0(a + a^\dagger)$, with $\delta i_0 = \omega_p\sqrt{\frac{\hbar}{2Z_p}}$ the zero-point current fluctuations and $Z_p = \sqrt{(L + L_J(\Phi_{Sq})/C_{sh}}$ the plasma mode impedance. Note that in addition the SQUID is biased by a dc current I_b so that the total current in the plasma mode is $I_b + i_p$.

The flux-qubit is clearly coupled to this plasma mode since it is the heart of its readout circuit. One of my postdoctoral achievements was precisely to derive the qubit-plasma mode coupling Hamiltonian, which turns out to be extremely peculiar and rich from the point of view of cavity QED. I will here only give the physical content, while the derivation can be found in [30]. With the SQUID biased at a certain dc current I_b, we are looking for the change in qubit energy induced by a small current fluctuation i_p in the plasma mode. The flux-qubit energy depends only on the phase γ_Q imposed over the 3 junctions, which in turn is governed by the current $J(I_b)$ circulating in the SQUID loop, rather than by its bias current. The key point then is that $J(I_b)$ is a *quadratic* function. This results in a Hamiltonian which has both a linear and quadratic coupling term, with the linear term strongly dependent on the value of I_b. One gets the total Hamiltonian (written in the FQ

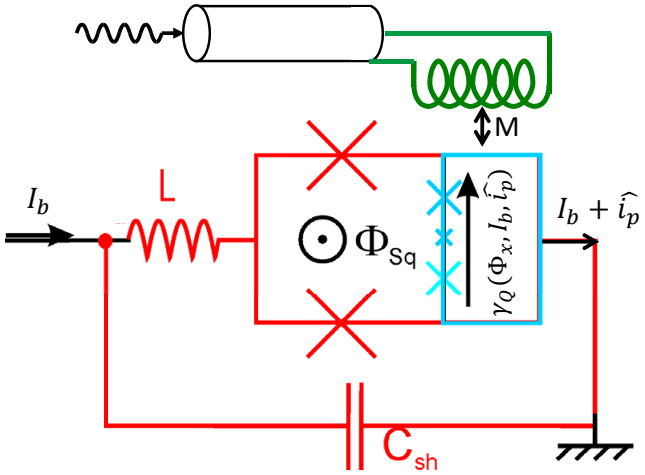

Figure 2.8: Qubit-plasma mode coupling. The plasma mode consists of the SQUID Josephson inductance $L_J(\Phi_{Sq}$ in series with the inductance L of the superconducting wires that connect it to the shunt capacitance C_{sh}. The total current through the SQUID is $I_b+\hat{i_p}$; the qubit bias point γ_Q depends on Φ_x, I_b and $\hat{i_p}$ yielding the qubit-plasma mode coupling. The qubit can be excited by an on-chip antenna to which it is coupled by a mutual inductance M and through which microwave pulses can be applied.

energy basis)

$$H/h = H_p + H_{FQ} + [g_1(I_b)(a + a^\dagger) + g_2(a + a^\dagger)^2](\sin\theta\sigma_x + \cos\theta\sigma_z) \qquad (2.12)$$

with the coupling constants $g_1(I_b) = (1/2)(d\lambda/dI_b)\delta i_0$ and $g_2 = (1/4)(d^2\lambda/dI_b^2)(\delta i_0)^2$, and $\lambda(I_b) = 2I_pMJ(I_b)/h$ [30]. Note that since $J(I_b)$ is essentially quadratic g_2 does not appreciably depend on I_b.

Comparing this interaction Hamiltonian with the simple Jaynes-Cummings case (Eq. 2.6), one notices two essential differences. First, the linear coupling term (equivalent to the dipolar electric coupling of Rydberg atoms to the microwave field) now has a coupling constant that can be tuned by a control parameter of the circuit by a very large amount as will be apparent below. Then, the coupling Hamiltonian also includes a term non-linear in the electromagnetic field, which is very unusual in cavity QED with real atoms where such a term would be usually negligible compared to the linear coupling. This is a good example of the richness and versatility that the electrodynamics of circuits brings to quantum physics.

2.2.3 Coherent dynamics of a flux-qubit coupled to a harmonic oscillator

Sideband transitions

The interest of the coupling Hamiltonian 2.12 becomes clear in the case where the qubit and plasma mode are largely detuned $|\delta| \gg g_1, g_2$ as was the case in our experiment. Indeed, by modulating the SQUID bias current it now becomes possible to modulate the linear coupling constant g_1 at a rate $\omega_p + \omega_0$ such that $g_1(t) = g_{10} + \delta g\cos(\omega_p + \omega_0)t$. Writing Eq. 2.12 in the interaction representation, keeping

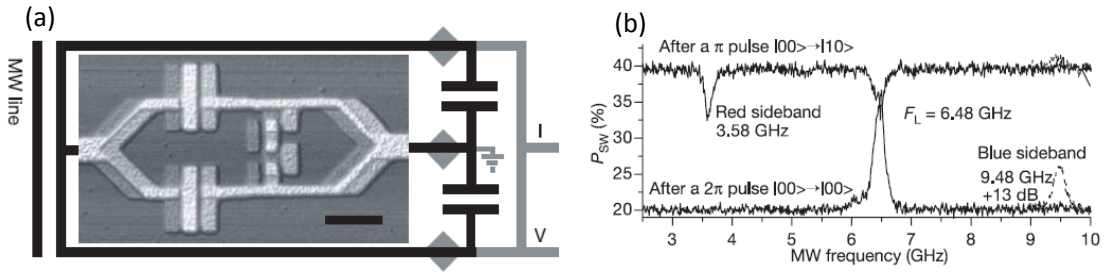

Figure 2.9: Qubit-plasma mode coupling : spectroscopy. (a) Atomic-Force Micrograph of the sample, showing the flux-qubit and SQUID loops. Scale bar is 1μm. *The SQUID is shunted by capacitor* C_{sh}*; gold quasi-particle traps (grey losange) are fabricated on each line. (b) Spectroscopic characterization of the energy levels after a* π *(upper scan) and a* 2π *(lower scan) Rabi pulse on the qubit transition. (extracted from [3])*

only the linear coupling term, and applying the rotating-wave approximation, one obtains

$$H_{BS}/h = \delta g \sin\theta (a\sigma_+ + a^\dagger \sigma_-) \tag{2.13}$$

which looks like an "anti-Jaynes-Cummings" Hamiltonian driving transitions in which both the oscillator and qubit change state coherently, in a correlated way. This is the exact analog of the situation encountered in ion-trap experiments [31], where the coupling to the oscillating motion of the ion can be modulated by a laser beam, allowing to drive the so-called sideband transitions. The modulation at $\omega_p + \omega_0$ is called the blue sideband resonance condition since this resonance occurs at a frequency higher than ω_p and ω_0. This transition is highly relevant for quantum information since it generates a coherent oscillations at frequency δg between states $|0,0\rangle$ and $|1,1\rangle$ (with $|i,j\rangle$ describing the FQ in $|i\rangle$ and the plasma mode in $|j\rangle$), and if stopped at a quarter period a maximally entangled state $(|00\rangle + |11\rangle)/\sqrt{2}$. Conversely, modulating g at $|\omega_p - \omega_0|$ (red-sideband resonance condition) yields a Jaynes-Cummings-like Hamiltonian allowing to drive oscillations between states $|0,1\rangle$ and $|1,0\rangle$.

Note that the idea applies more generally. If two circuits are coupled by a coupling constant that can be tuned by a control parameter λ as is often possible using SQUIDs as coupling elements, then it is possible to induce sideband transitions and therefore to entangle them. The interest of this scheme compared to cavity QED is that the coupling is ON only when λ is modulated, which is very conveniently achieved at microwave frequencies. We called this coupling scheme parametric coupling [32].

Experimental results : sample description

These ideas were tested in a series of experiments reported in [3] on a flux-qubit sample. A micrograph of the flux-qubit + SQUID loops is shown in Fig. 2.9a, together with a schematics of the plasma mode and readout circuit. From the sample design one expects the plasma mode frequency to be $\omega_p/2\pi \approx 3\,\text{GHz}$ and $Q \approx 100$. The flux-qubit has a gap $\Delta = 5.9\,\text{GHz}$ and persistent-current $I_p = 275\,\text{nA}$.

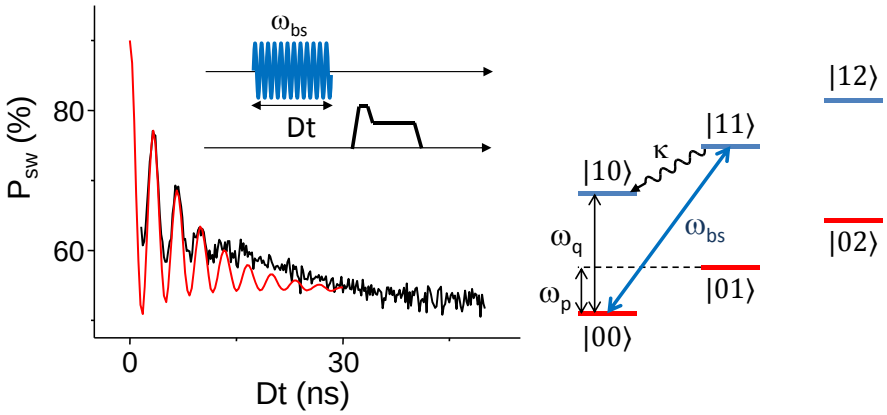

Figure 2.10: Coherent dynamics on the blue sideband. Black solid lines : Measured $P_{sw}(Dt)$, Dt being the duration of a microwave pulse at ω_{bs}. Note that in this sample and at this bias point, the SQUID switching probability is reduced when the qubit is in the excited state, contrary to the data shown in Fig. 2.9. Red solid line : result of the integration of a master equation describing the dynamics of the coupled system, with the energy levels shown on the right panel (unpublished).

Experimental results : spectroscopy of the coupled system

The qubit-plasma mode coupling was first observed spectroscopically, by applying microwave pulses of varying frequency to the microwave line coupled inductively to the qubit, followed by a qubit readout pulse. Typical data can be seen in Fig. 2.9. Starting from the qubit in the ground state, we see that in addition to the main qubit peak at ω_0, another peak is seen at higher frequency that we call ω_{bs}. We also performed spectroscopy starting with the qubit in the excited state instead, by applying a π pulse on the qubit before spectroscopy. In this case, in addition to the main qubit peak a dip is found at a lower frequency ω_{rs}, with $|\omega_{bs} - \omega_0| \approx |\omega_0 - \omega_{bs}|$.

These results are readily explained looking at the energy level scheme shown in Fig. 2.10. The plasma mode being at 3 GHz is expected to be close to its ground state at 30 mK. Starting from $|0,0\rangle$, only the blue sideband can be excited, giving rise to the high-frequency peak. But starting from $|1,0\rangle$ only the red sideband can be excited this time, which gives rise to qubit de-excitation and therefore to a low-frequency dip in P_{sw}, as observed in the data. Other measurements, reported in [3], make it possible to unambiguously identify the coupled mode as the plasma mode of the SQUID as described above.

Experimental results : sideband dynamics

We now turn to results showing the coherent dynamics of this coupled qubit-oscillator system. In Fig. 2.10 are shown measurements of the qubit excited state population while applying microwave pulses of varying length Dt at the blue sideband frequency ω_{bs}.

Damped oscillations are observed which remarkably do not converge towards $P_e = 1/2$ as is the case for a usual Rabi oscillation but instead towards $P_e = 1$. This can be understood from the level scheme shown in Fig. 2.10, by noting that the plasma mode damping rate $\kappa \approx (10\text{ns})^{-1}$ is much faster than the qubit damping rate $T_1^{-1} \approx (4\mu\text{s})^{-1}$. As a result, driving the blue sideband efficiently pumps the

system into $|10\rangle$, similar to optical pumping. This is confirmed by the results of a master equation simulation of the system, also shown in Fig. 2.10. In the course of these sideband Rabi oscillations the FQ and plasma mode become entangled, even if it would be necessary to measure both systems independently in order to prove it, which is impossible in the circuit as it is.

Discussion of the sideband excitation mechanism

Before concluding this part on blue and red sideband transitions in a coupled flux-qubit-plasma mode system, it is worth having a short technical discussion about the exact mechanism allowing sideband excitation in our sample, in the goal of correcting a probable mistake in our original article [3]. Indeed at that time we attributed the sideband excitation to direct driving via the qubit, and not I_b-modulation as discussed earlier in this paragraph. Theoretically [33, 34] it is indeed possible to drive the sideband resonances by directly driving the qubit at ω_{bs} or ω_{rs}, an alternative mechanism to the more complex parametric driving discussed earlier in this chapter. However a more detailed look at the predictions shows one inconsistency with our measurements: both [33, 34] predict that this direct driving mechanism is only possible if an interaction term between the qubit and the resonator of the form $(a + a^\dagger)\sigma_z$ is present in the Hamiltonian (with σ_z referring to the qubit energy eigenstates). As seen from Eq. 2.12 such a term is indeed present in the qubit-plasme mode Hamiltonian, *except when the qubit is biased exactly at its optimal point*. There, the coupling is purely transverse, and it should therefore not be possible to drive the sidebands (two-photon driving is nevertheless possible [34, 35]). In the experiment we saw no sign that the sideband driving amplitude is reduced in the optimal point vicinity.

At the time of these measurements and of the paper publication we did not pay attention to this problem; but later I noticed this inconsistency, and this pushed me to develop the idea of parametric driving [32] as a probable explanation for our observations. Indeed, because of the sample geometry it is unavoidable that the microwave pulses generated in the microwave line to drive the qubit also induce a flux modulation in the plasma mode leading to a modulation of the bias current I_b at the frequency of the microwave drive. Estimates indicate that a modulation of order 100 nA would be sufficient to explain the measurements which would be reached at microwave powers similar to the ones used in the experiment. Despite this probably erroneous interpretation of the exact sideband excitation mechanism, the data reported in [3] represent the first experimental evidence for the strong coupling of a superconducting qubit to a harmonic oscillator; they were published back-to-back with the ground-breaking results of A. Wallraff in R. Schoelkopf group at Yale observing the vacuum Rabi splitting of a coupled qubit-resonator system, in a system described in more details in the next chapter. We also note that sideband transitions were later used in A. Wallraff group at ETH to perform a full two-qubit gate between two transmon qubits [35] and have now become a widespread concept in circuit QED.

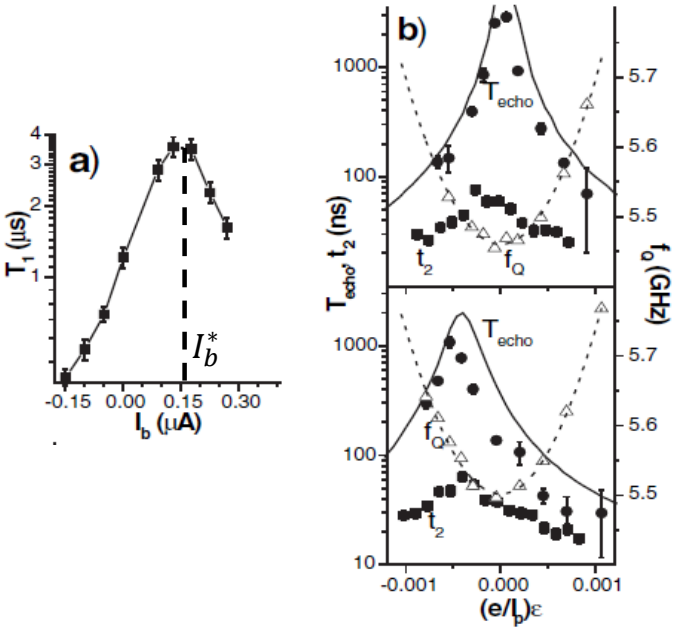

Figure 2.11: Decoherence of flux-qubit caused by its coupling to the plasma mode. (a) Dependence of the energy relaxation time T_1 on I_b (at the optimal point $\Phi_x = \Phi_0/2$, showing that outside of I_b^* (marked by dahsed line on the figure) T_1 is limited by spontaneous emission in the detection waveguide. (b) Dependence of the spin-echo time T_{echo} and dephasing time t_2 on the qubit bias ϵ for $I_b = I_b^*$ (top) and $I_b = 0\,nA$ (bottom). Solid black line is the prediction of Eq. 2.14 for a temperature of 70 mK, without any adjustable parameter. The qubit frequency is shown as a triangle together with the spectroscopy fit in dashed line.

2.2.4 Qubit decoherence induced by coupling to the plasma mode

The strong coupling of the flux-qubit to the plasma mode can lead to its decoherence. This can occur in two different ways : (i) the qubit can lose its energy by spontaneous emission of a photon into the measurement line via the plasma mode (so-called Purcell effect) (ii) fluctuations of the photon number in the resonator can induce corresponding fluctuations of the qubit frequency, leading to qubit dephasing. To study these effects, we have measured the coherence properties of a flux-qubit sample for various bias parameters : SQUID bias current I_b and qubit flux-bias ϵ [6, 30].

Energy relaxation via the plasma mode

The dependence of the flux-qubit energy relaxation time T_1 as a function of I_b while keeping the qubit at precisely the same frequency is shown in Fig. 2.11a. The data show that T_1 changes by more than an order of magnitude when I_b is varied, being maximal at a current that we called the *decoupling current* I_b^*. In order to understand these results from the point of view of the coupling Hamiltonian 2.12 we have performed extensive spectroscopic measurements of the flux-qubit which enabled us to directly measure all the Hamiltonian parameters as explained in [6, 30]. They indicate that the current I_b^* corresponds precisely to the current for which the linear coupling term in Eq. 2.12 vanishes : $g_1(I_b^*) = 0$. This shows that for $I_b \neq I_b^*$

at least, the qubit energy relaxation is indeed caused by spontaneous emission via the plasma mode.

Dephasing by photon number thermal fluctuations

As regards qubit dephasing, I developed a model [30] describing the dephasing of a qubit coupled to a harmonic oscillator with mean thermal photon number n_{th} causing a qubit frequency shift $2\pi\delta\nu_0$ per photon in the oscillator. In the limit where $2\pi\delta\nu_0 \ll \kappa$ (the harmonic oscillator energy damping rate), I found that the qubit dephasing time is

$$\tau_\phi = \frac{\kappa}{n_{th}(n_{th}+1)(2\pi\delta\nu_0)^2}. \tag{2.14}$$

If $\delta\nu_0$ is large, this can result is strong dephasing as discussed below. This photon-noise model contributed to a better understanding of decoherence in superconducting qubits in several other experiments [36, 37, 38], and was recently generalized to an arbitrary ratio between $\delta\nu_0$ and κ [39].

In our case $\delta\nu_0$ is not given by the simple Jaynes-Cummings formula because of the more complex form of the coupling Hamiltonian 2.12 which contains one linear and one quadratic term in the field. The linear term causes a frequency shift by application of second-order perturbation theory to the term $(a + a^\dagger)\sigma_x$ (without rotating wave approximation, not valid here). The quadratic term however leads to a frequency-shift per photon at the first order of perturbation theory because of the term $a^\dagger a\sigma_z$. In total, for a flux-qubit coupled to the SQUID plasma mode, we obtain

$$\delta\nu_0 = 4[(g_1(I_b)\sin\theta)^2 2\pi\frac{\omega_q}{\omega_q^2-\omega_p^2} - g_2\cos\theta]. \tag{2.15}$$

Combining formulas 2.14 and 2.15 yields quantitative predictions of the flux-qubit dephasing time, the only adjustable parameter of the model being the temperature of the plasma mode, that we compared to measurements of the flux-qubit coherence times with spectroscopic measurements and spin-echo sequences as a function of I_b and ϵ shown in Fig. 2.11b.

The best coherence times (with a spin-echo time $T_E = 4\mu$s) are obtained for $I_b = I_b^*$ and $\epsilon = 0$, which is an optimal point for the flux-qubit as regards flux-noise, bias current noise, and thermal photon noise [6]. Note that the measured values of T_1 and T_E were remarkably long for superconducting qubits at that time, remaining a world record until 2009 [40] and the later development of a new generation of qubits with longer coherence times [37]. Outside of this optimal point, we find that a quantitative agreement between the measured coherence times and the photon-noise model if we inject a plasma mode effective temperature of 70 mK, slightly higher than the cryostat temperature but plausible for this type of experiments.

2.2.5 Flux-qubit : Summary and Perspectives

As seen earlier in this section, the work with flux-qubits performed during my post-doc revealed an aspect that had been somewhat overlooked so far in the field of superconducting circuits: the importance of properly modeling and understanding the coupling of the qubit to its detection circuit. Coupling the flux-qubit to the

plasma mode via a dc SQUID was shown to yield a rich Hamiltonian, which enabled the observation of coupled dynamics between the two systems. The tunability of this coupling allowed also to demonstrate unambiguously that its fluctuations were responsible for qubit decoherence around the optimal point. In demonstrating and understanding these effects, my PhD experience in cavity quantum electrodynamics with Rydberg atoms was essential, since a quantized description of the plasma mode and of its coupling to the qubit was key. In a sense these results, obtained in parallel with the pioneering experiments of Andreas Wallraff and Rob Schoelkopf at Yale, marked the transition between early superconducting qubit experiments which were treated in the framework of mesoscopic physics and a new generation of experiments which required advanced quantum optics treatment. It also led us to realize that, while it is utterly difficult to achieve strong coupling between real atoms and electromagnetic cavities, artificial superconducting atoms tend to be strongly coupled to oscillators in their environment, even in circuits that were not designed in that purpose. These aspects will be more developed in the next chapter which deals with a next generation of experiments performed with all-microwave measurements, following the path opened by R. Schoelkopf group at Yale.

It is also timely to briefly assess the present status of flux-qubit research. From a quantum information viewpoint, the flux-qubit suffers from two drawbacks : (i) its coherence times are long only at the optimal point (ii) the flux-qubit frequency at this optimal point (the gap Δ) is difficult to predict due to its exponential dependence on the size of the small Josephson junction. An interesting solution is to make Δ tunable, by turning this small qubit junction into a SQUID as demonstrated in [41]; this however requires an additional local control line which complicates the chip design. Compared to transmon qubits (described in the next chapter), the flux-qubit appears in present days as a more complex circuit whose coherence times are slightly inferior. It is therefore not the qubit of choice for present designs of large-scale (≈ 100 qubits !) quantum processors.

Nonetheless, flux-qubits have a truly unique property : their magnetic dipole is by far the largest of all qubit designs. Certain specific applications can greatly benefit from this enormous dipole. In particular flux-qubits have a bright future in hybrid quantum circuits aiming at coupling spins to superconducting circuits, as shown by several proposals [42] and experiments [43]. This is the focus of one of our ongoing projects (led by Michaël Stern presently postdoc in the group), whose long-term goal is to reach the strong coupling regime between a single spin and a flux-qubit. For this purpose a first preliminary step was to obtain flux-qubits with reproducibly long coherence times. We revisited the flux-qubit readout with a circuit QED approach and obtained coherence times significantly enhanced compared to the results presented in this chapter, of order $5-20\mu$s [44], which is encouraging for the future of the project.

Chapter 3

Circuit QED with Transmon Qubits

This chapter describes work performed since I joined the Quantronics group, first as a postdoc ($2005-2006$) then as a permanent researcher. At the time that I arrived, it was becoming clearer and clearer that the circuit QED experiments performed in R. Schoelkopf group at Yale University were a major breakthrough for the field of quantum circuits, in particular because qubit readout by microwave probing of the cavity is much less invasive for the qubit than dc switching of a Josephson junction to the voltage state. Together with Denis Vion and Daniel Esteve we quickly decided that I would start developing a similar research line in the Quantronics group, and I supervised PhD student Agustin Palacios-Laloy to do that.

One of the interests of the circuit QED setup is to make it possible to vary the strength of the measurement, from weak to projective, simply by changing the power of a microwave source. Motivated by proposals by A. Korotkov, this suggested us to study this transition in the context of circuit QED. As a final goal of this project we were able to perform for the first time a thought experiment proposed by A. Leggett and A. Garg in 1985 and to test their proposed inequality [45], which brought further confirmation that superconducting circuits, despite their macroscopic character, do behave quantum-mechanically [7].

3.1 System description

In order to develop novel circuit QED experiments, our starting point was to reproduce the remarkable results obtained in R. Schoelkopf group. Two major breakthroughs came from that group : circuit QED with microwave measurements [46, 4, 47], and a new qubit design called the transmon [48, 49]. In this section we will describe our implementation of circuit QED with transmon qubits, again strongly inspired by the work at Yale.

The core of circuit QED experiments is shown in Fig. 3.1: a superconducting qubit of the transmon type (in purple) is capacitively coupled to a coplanar waveguide (CPW) superconducting resonator (in green). The resonator consists in a CPW transmission line of length L interrupted in two points, giving rise to Fabry-Pérot resonances at frequencies $\pi\bar{c}/L$, with $\bar{c}$ the speed of light in the waveguide.

The perfect analogy with cavity QED (see Fig.1 of previous chapter) is visible at first sight, with the superconducting qubit playing the role of the Rydberg atom and

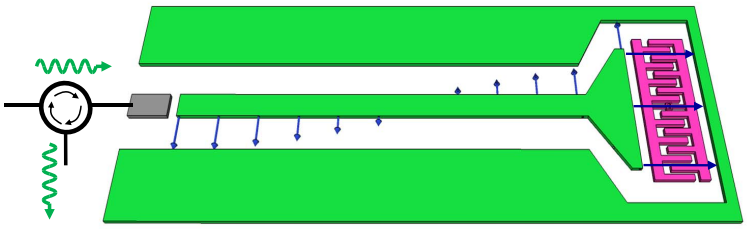

Figure 3.1: Circuit QED principle. A transmon qubit (in purple) is capacitively coupled to a coplanar waveguide (CPW) resonator (in green). The coupled system is probed and driven by microwave pulses at the resonator input.

the CPW resonator the role of the high-Q cavity. While in cavity QED the atoms were used to as a probe of the cavity field, in circuit QED the resonator, probed by microwave signals reflecting at the cavity input (see Fig. 3.1), is used to infer the state of the qubit. The essentials of this system are described in this paragraph, while more details can be found in several references [50, 8].

3.1.1 The transmon qubit

The transmon qubit is the modern version of one of the major qubit designs, the Cooper-pair box (CPB). Its circuit diagram is shown in Fig. 3.2. It consists of an isolated Josephson junction of critical current I_C in parallel with a shunting capacitor C. The physics of the CPB is governed by two energy scales : the Josephson energy $E_J = I_C\Phi_0/2\pi$ which quantifies the pairing energy gained by tunneling between the two superconducting islands of the CPB, and the charging energy $E_C = e^2/2C$ giving the cost in energy of charging the capacitor C with one electronic charge. Early CPBs (in particular in Nakamura's pioneering experiment [25]) were in the regime $E_J \ll E_C$ where they are highly sensitive to charge noise; the Quantronium CPB was in a regime $E_J \approx E_C$ where coherence times can be rather long at the charge optimal point. The transmon is a CPB with $E_J \gg E_C$ (typically $E_J/E_C = 50$), which yields an exponential suppression of charge noise sensitivity [48].

The simplest way to understand the transmon qubit basic properties is to treat the Josephson Hamiltonian $-E_J \cos\phi$, ϕ being the phase across the junction, in perturbation theory. This is possible for a transmon, since in the $E_J/E_C \gg 1$ regime the quantum fluctuations of the phase around its equilibrium value are $\ll 1$ so that $\cos\phi$ can be expanded in powers of ϕ. Together with the charging energy the total Hamiltonian of the transmon qubit can thus be written as

$$H = 4E_C\hat{n}^2 - E_J(1 - \frac{\phi^2}{2} + \frac{\phi^4}{24}), \tag{3.1}$$

with $\hat{n}$ the number of Cooper-pairs having tunneled through the junction, which is conjugate variable to ϕ $[\hat{\phi}, \hat{n}] = 1$. The first three terms describe a simple harmonic resonator, with inductance $L_J = \phi_0^2/E_J$ and capacitance C ($\phi_0 = \hbar/2e$ being the reduced flux quantum). The fourth term makes this resonator non-linear. Using the field creation and annihilation operators b and $b^\dagger$ and keeping only the secular terms yields

$$H/\hbar = \omega_0 b^\dagger b + \frac{K}{2}(b^\dagger)^2 b^2, \tag{3.2}$$

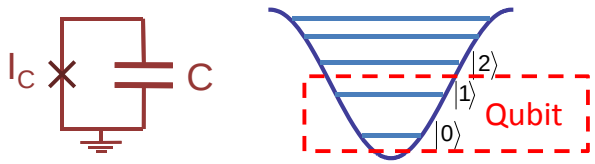

Figure 3.2: Transmon qubit principle. (left) Electrical scheme. The transmon consists of a Josephson junction (here shown as a cross) in parallel with a shunting capacitor. (right) The transmon energy levels are those of a weakly nonlinear resonator, so that the two lowest levels form a qubit.

with $\omega_0 = 1/\sqrt{L_J C}$ and $K = E_C/\hbar$. The corresponding transmon energy spectrum is shown schematically in Fig. 3.2: successive levels have an energy difference $E_{n+1} - E_n \equiv \hbar\omega_{n,n+1} = \hbar[\omega_0 + [n + 1/2]K]$. They are thus non-equidistant, and if the anharmonicity parameter K is large enough the two lowest levels form a qubit. Typical parameters are $\omega_0/2\pi \approx 6\,\mathrm{GHz}$ and $K/2\pi = 300\,\mathrm{MHz}$, implying that as long as the transmon is driven at low enough Rabi frequency it will indeed behave as a two-level system. Restricted to the $|0\rangle - |1\rangle$ subspace the transmon artificial atom Hamiltonian is thus $H_{at} = -\omega_q\sigma_z/2$, with $\omega_q = \omega_0 + K/2$.

Compared to the CPB and the FQ, the transmon has one major advantage. It does not need to be biased at a specific working point by a DC control parameter. As a result the transmon is a very robust qubit design, and it is possible to obtain coherence times in the hundreds of nanoseconds without big effort.

3.1.2 Transmon coupled to a CPW resonator

In the circuit QED setup shown in Fig. 3.1, the transmon is capacitively coupled to a CPW resonator of characteristic impedance Z_0 with a coupling capacitor C_c. This is the exact equivalent of the dipole electric Hamiltonian coupling a Rydberg atom to the resonator in the Cavity QED setup. This qualitative argument can be turned into a rigorous derivation [46, 50, 48], showing that the coupled system Hamiltonian is indeed the Jaynes-Cummings Hamiltonian of Cavity QED

$$H/\hbar = -\frac{\omega_q}{2}\sigma_z + \omega_r a^\dagger a + g(a^\dagger\sigma^- + a\sigma^+). \tag{3.3}$$

The coupling constant is given by $\hbar g = \beta\delta V_0|\langle 0|\hat{Q}_q|1\rangle|$ [46], with $\beta = C_c/C$, $\delta V_0 = \omega_0\sqrt{\hbar Z_0/\pi}$ the voltage zero-point fluctuations, and $|\langle 0|\hat{Q}_q|1\rangle|$ the charge matrix element of the transmon qubit which can be quantitatively computed for precise parameters but is of order $2e$.

To determine whether the system is in the strong coupling regime, one can evaluate the coupling constant g and compare it to the various damping rates. With $\delta V_0 = 2 - 3\,\mu\mathrm{V}$, $\beta \approx 0.2$, and $|\langle 0|\hat{Q}_q|1\rangle| \approx 2e$, one gets $g/2\pi \approx 250\,\mathrm{MHz}$. All typical damping rates (at least the damping caused by uncontrolled internal losses) being of order $\approx 100\,\mathrm{kHz}$, the qubit - resonator coupling constant is several orders of magnitude large enough so that the strong coupling regime is reached.

Note that compared to the coupling of a FQ to the plasma mode of its readout SQUID as discussed in the previous chapter, we have a less rich Hamiltonian; in particular the coupling constant g is not tunable in this case. However this also yields a more robust system: whereas in the FQ sample discussed in the last chapter

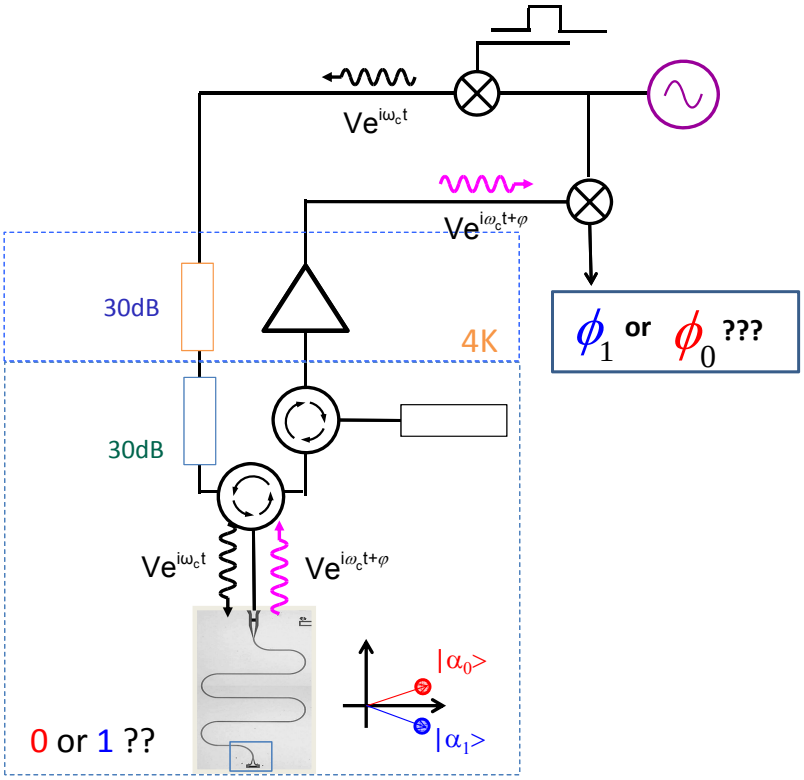

Figure 3.3: Qubit readout principle. Microwave pulses at the qubit resonance frequency are sent down input lines (heavily attenuated at low temperatures), generate a field inside the resonator with a phase that depends on the qubit state due to dispersive coupling, and are reflected in the output line. After amplification the reflected pulse phase is measured by homodyne demodulation yielding the qubit state.

both the SQUID bias current and the flux threading the qubit had to be set at a very precise value to benefit from the best properties of the circuit, the transmon - circuit QED setup needs no special tuning. This robustness enabled the superconducting qubit community to move from performing experiments dedicated to either have a qubit work or study how it works, to experiments in which the qubit in itself is no longer a research topic but a tool for research on quantum physics or quantum information. This is because of this robustness and simplicity that we decided to use the transmon-circuit QED system for our future experiments in the group.

3.1.3 Qubit state manipulation and readout

One of the key advantages of the circuit QED setup developed in R. Schoelkopf group is the possibility of performing single-qubit rotations as well as qubit state readout with microwave pulses sent at the input of the CPW resonator. Qubit state manipulation is done using a microwave pulse at the qubit frequency ω_q; by varying the amplitude and phase of this pulse arbitrary rotations on the Bloch sphere can be achieved. Qubit state readout is performed at the end of each experimental sequence, by sending a microwave pulse at the cavity frequency ω_c, and measuring the reflected phase. A schematics of the readout process is shown in Fig. 3.3.

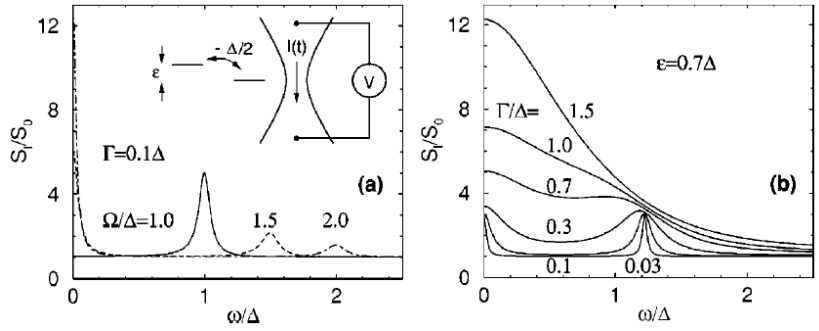

Figure 3.4: Double-dot experiment proposed by Korotkov [52]. A double dot with tunneling amplitude Δ and detuning ϵ is measured by the current through a neighboring Quantum Point COntact (QPC). (a) Predicted spectrum of the QPC current, showing a peak at the Rabi frequency $\Omega = \sqrt{\Delta^2 + \epsilon^2}$. (b) Dependence of the Rabi peak shape on the measurement rate Γ [52]

3.2 Weak measurements, Quantum Zeno effect, and test of the Leggett-Garg inequality

3.2.1 Background

In quantum mechanics, the measurement of an observable always imparts a very peculiar back-action on the measured system, summarized by the wave-function collapse postulate which states that (i) the measurement outcome is an eigenvalue of this observable, with a probability determined by the system quantum state prior to the measurement, and (ii) the system quantum state is irreversibly projected onto the corresponding observable eigenstate. For some types of measurements this projection occurs instantaneously, as is the case for the detection of an optical photon by a photo-detector, a prototypical measurement for quantum optics. But for other types of measurements, acquiring enough information for resolving the observable eigenstates takes a time sufficient that an experimentalist can "zoom in" and try to observe in direct the projection occurring. With such weak continuous measurements, every time increment brings slightly more information about the system (together with some randomness), which causes a slight drift of the system quantum state determined by the measurement outcome. The evolution of the system is best described by a stochastic master equation which takes into account both the system Hamiltonian evolution, its damping, the random measurement outcome, together with the quantum back-action of this continuous measurement record, yielding "quantum trajectories" that have long been studied in quantum optics [51].

On this topic of continuous measurements and of the quantum back-action, several interesting theoretical predictions were made by Alexander Korotkov. He was the first physicist to dare to apply advanced quantum optics concepts such as quantum trajectories to solid-state mesoscopic devices, at a time where the convergence of atomic and solid-state quantum physics was far from being evident. In all his articles, Korotkov considered a system consisting of a double quantum dot (DQD) in a 2D electron gas (see Fig. 3.4), loaded with one electron that can tunnel between the left and the right dot, which can be modelled as a two-level system (TLS) with a σ_z observable corresponding to the presence of the dot in either dot. The DQD is capacitively coupled to a quantum point contact (QPC) in such a way that the tunnel

barrier is slightly modified depending on which dot the electron is actually located. Electrons passing through the QPC thus perform a weak continuous measurement of σ_z. One of the first predictions of A. Korotkov in this system was that the current through the QPC would carry a spectral signature of the quantum dynamics of the electron in the QDQ : namely, a peak at the frequency corresponding to the tunneling of the electron between the two dots should be oberved, the so-called Rabi peak as can be seen in Fig. 3.4 [53, 52].

The interesting non-trivial aspect of this prediction was that left to itself (that is, unmeasured), the electron in the DQD would quickly relax towards the ground state of its Hamiltonian, namely an eigenstate of the σ_x operator consisting of an equal weight superposition of the electron being in the left and right dot, a state which by essence is entirely stationary and in which all dynamics is suppressed. However, even the weakest current passing through the QPC performs a weak measurement of σ_z, an observable which does not commute with the Hamiltonian, and is thus sufficient to generate some dynamics in the electron state through its quantum back-action, giving rise to the Rabi peak. Korotkov provided detailed predictions about the width of the Rabi peak, and its evolution when the measurement strength (governed by the voltage bias across the QPC) is increased. He pointed out in particular a crossover that should occur when the measurement strength becomes comparable to the tunneling in the DQD (that is between a weak and a strong measurement): the peak at the tunneling frequency should evolve progressively into a Lorentzian peak centered at zero frequency (see Fig. 3.4b). Korotkov made also important predictions regarding the maximum possible signal-to-noise of the Rabi peak allowed by quantum mechanics [52]. He then made the connection between the spectral weight of this Rabi peak and a long-standing prediction by Tony Leggett [54], to which we will come back below. And finally, he proposed several quantum feedback schemes aimed at stabilizing the phase of the Rabi oscillations [55, 56].

The predictions of Korotkov have still never been tested in the system he considered, for several reasons: first, Korotkov neglected the fact that the dc current passing through a quantum dot is very far from being measured at the quantum limit; then DQDs are subject to charge noise which shortens their coherence times, so that coherent tunneling rates need to be in the few GHz, which in turn requires colossal detection bandwidth of the QPC current, very far from any realistic measurement system. My contribution was to realize in 2006 (following several discussions with H. Mooij and A. Lupascu in Delft who introduced me to this topic) that instead of an electron tunneling between two quantum dots and measured by the current through a QPC, a superconducting qubit driven by a microwave signal and measured at the same time dispersively by a coplanar waveguide resonator in circuit QED was the ideal testbench for Korotkov ideas and predictions. Indeed, the dispersive measurement is quantum non-destructive since the dispersive Hamiltonian commutes with the qubit σ_z operator, and its strength can be very easily varied by changing the mean photon number in the cavity $\bar{n}$. This led us to a series of experiments, described in the following, in which we verified some of Korotkov's predictions by observing the Rabi peak, and testing the Leggett-Garg inequality [45] using weak measurements. Later, building on our work, other groups pushed the circuit QED implementation of Korotkov ideas even further thanks to the development of parametric amplifiers, and managed to go up to the implementation of the quantum feedback schemes [57, 58].

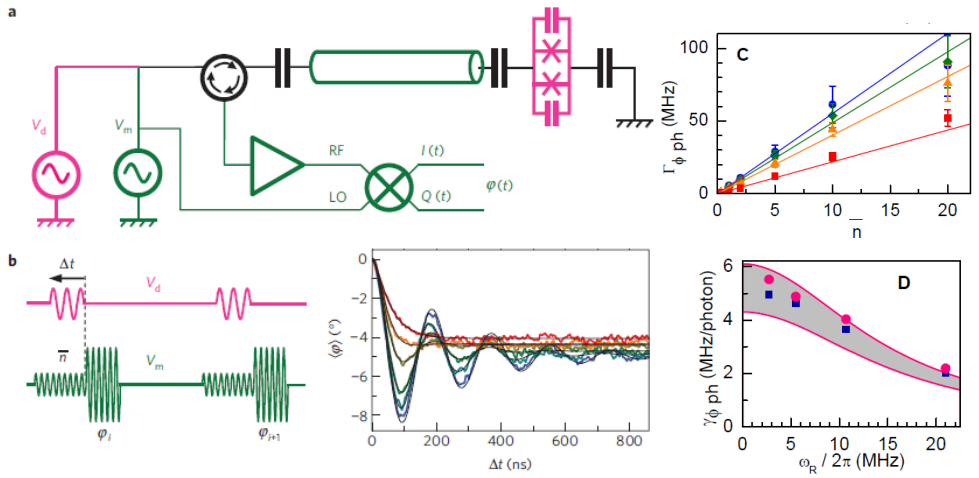

Figure 3.5: Ensemble-averaged Rabi oscillations. (a) Experimental setup. (b) (left) Pulse sequence to measure ensemble-averaged Rabi oscillations in the presence of a weak measurement pulse in the cavity. (right) Experimental ensemble-averaged Rabi oscillations with respectively $\bar{n} = 0, 1, 2, 5, 10,$ and 20 photons in the cavity, showing the progressive dephasing of the Rabi oscillations up to an exponential decay. (c) Extracted measurement-induced dephasing rate $\Gamma_\phi(\bar{n})$ showing the expected linear dependence in $\bar{n}$. (d) (pink dots) Dephasing rate per photon as a function of Ω_R, together with theoretical predictions (gray area) and simulation results (blue squares).

3.2.2 Experimental Setup

For our implementation of these ideas, we used the experimental setup shown in Fig. 3.5. A trasmon qubit is coupled dispersively to its readout resonator with dispersive coupling constant $\chi/2\pi = 1.75\,\text{MHz}$. The cavity damping rate is $\kappa/2\pi = 30\,\text{MHz}$, placing the experiment largely in the regime where $\chi \ll \kappa$ as needed for weak measurements. It is driven by a microwave source V_d at its resonance frequency. Measurements are performed with another microwave source V_m at the cavity frequency ω_c which builds up an intra-cavity field with mean photon number $\bar{n}$. The field reflected on the cavity is routed by a circulator to a cryogenic amplifier, before being detected by homodyne demodulation with a local oscillator at the same frequency, yielding its in-phase and out-of-phase quadratures $I(t)$ and $Q(t)$ with a bandwidth $\approx 100\,\text{MHz}$.

In this low-quality factor regime, it can be shown that the output quadratures (noted $X = I, Q$) are directly proportional to the qubit excited state population : $X(t) = \bar{X} + (\delta X/2)\langle\hat{\sigma_z}\rangle_c(t) + \xi_0(t)$, where $\langle\hat{\sigma_z}\rangle_c(t)$ is the expectation value of $\hat{\sigma_z}$ at time t conditioned on the whole history of the detector outcome $X(t')$ for $t' \leq t$, δX is the maximum detector signal proportional to the measurement amplitude $\sqrt{\bar{n}}$, and $\xi_0(t)$ is the total output noise of the amplifier. When both the drive and the measurement pulses are on, the state of the qubit evolves under 2 conflicting influences : (i) the effect of the drive which tends to mix the σ_z eigenstates (ii) the quantum back-action of the measurement pulse, which tends to project it on a σ_z eigenstate. Depending on the ratio between the driving strength (characterized quantitatively by the Rabi frequency Ω_R) and the measurement strength (characterized quantitatively by the inverse of the minimum measurement time needed to discriminate the two system states with a quantum-limited amplifier $\Gamma_{meas} = 8n\bar{\chi^2}/\kappa$), the system

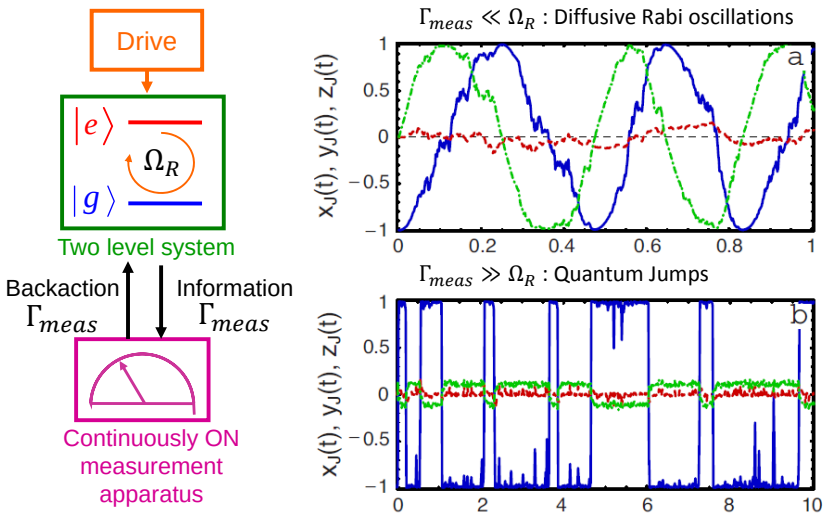

Figure 3.6: Principle of our weak measurement experiment. (left) The two-level system is at the same time driven at frequency Ω_R and measured with a strength Γ_{meas}, which also causes a quantum back-action. (right) Examples of quantum trajectories [59] in the diffusive Rabi limit $\Omega_R \gg \Gamma_{meas}$ (top) and the quantum jump limit $\Omega_R \ll \Gamma_{meas}$ (bottom).

will have qualitatively different types of quantum trajectory : either a diffusive Rabi oscillation if $\Omega_R \gg \Gamma_{meas}$ or incoherent quantum jumps between σ_z eigenstates if $\Omega_R \ll \Gamma_{meas}$. This complex dynamics is described by a stochastic master equation (see in particular [53, 59]). Typical trajectories in the two regimes (extracted from [59]) are shown in Fig. 3.6, together with a summary of the principle of the experiment.

3.2.3 Ensemble-averaged Rabi oscillations in the presence of a weak measurement

We start with a series of calibration experiments in which we measure standard ensemble-averaged Rabi oscillations, in the presence of a weak measurement pulse in the cavity. In ensemble-averaged experiments, the back-action of the measurement, which projects each time on a different eigenstate due to the randomness of the measurement process, appears simply as an extra dephasing term in the qubit dynamics. It was measured spectroscopically in circuit QED in [60]. A semi-classical description of this dephasing process is that the intra-cavity photon number fluctuates due to shot-noise, which in turn induces fluctuations of the qubit frequency and therefore dephasing, similar to the thermal photon noise encountered in the previous chapter. The predicted dephasing rate is $\Gamma_\phi = 8\bar{n}\chi^2/\kappa$ [8], with a dependence on $\bar{n}$ which can be understood by the photon number variance scaling like $\sqrt{\bar{n}}$ for a coherent state of the electromagnetic field.

The experimental protocol shown in Fig. 3.5b consists in repeating 10^4 identical sequences of (i) waiting a time long enough that the qubit has relaxed in its ground state (ii) applying a microwave pulse of duration Dt at ω_q in presence of a weak microwave drive in the cavity, populating it with $\bar{n}$ photons on average (iii) Turning off the qubit drive and performing a projective measurement of the qubit state, yielding an average signal phase ϕ_i.

For $\bar{n} = 0$ the phase of the reflected signal shows damped Rabi oscillations as expected, with a damping time governed by the qubit intrinsic relaxation time $T_1 = 200\,\text{ns}$ probably limited by dielectric losses in the transmon shunting capacitor. Increasing $\bar{n}$, the Rabi oscillations damping time becomes shorter, up to the point where the Rabi oscillations vanish and give place to an exponential damping. Fitting these data with analytical solutions of the Bloch equations, we extract a measurement-induced dephasing rate $\Gamma_\phi(\bar{n})$ in quantitative agreement with the predicted $8\bar{n}\chi^2/\kappa$ (see Fig. 3.5) as long as the Rabi frequency is smaller than the cavity bandwidth κ. Note that as can be seen in Fig. 3.5, once the qubit evolution has become exponential, increasing the measurement strength further makes the exponential time constant longer and longer. This is a manifestation of the quantum Zeno effect: a strong measurement inhibits the transition between ground and excited states.

3.2.4 Continuous monitoring of Rabi oscillations : the Rabi peak

In order to observe a measurement back-action that goes beyond a simple extra dephasing term with a semi-classical intepretation, one needs to measure not the ensemble-averaged detector output signal but instead higher-order correlation functions. For that, we monitor the system in its steady-state, long after the transient ensemble-averaged Rabi oscillations such as shown in Fig. 3.5 are washed out. Instead of applying microwave pulses, the two sources V_d and V_m are continuously ON. The measurement of the two-time detector output signal $K_X(\tau) = \langle (X(t) - \bar{X})(X(t+\tau) - \bar{X})\rangle/(\delta X/2)^2$ is difficult in our setup because the amplifier noise dominates the output signal. However this added noise can be removed by processing the signal in the frequency domain.

For that, we compute the square modulus S_I and S_Q of the Fourier transforms of $I(t)$ and $Q(t)$, to obtain the detector output power spectrum $S(\omega) = S_I(\omega) + S_Q(\omega)$. The signal power spectrum is then obtained by subtracting the amplifier noise spectrum $S_{OFF}(\omega)$ measured when the two sources V_d and V_m are OFF from the signal-plus-noise spectrum $S_{ON}(\omega)$ measured with both sources ON, and by dividing this difference by the independently calibrated frequency response of the measurement lines and setup. Typical curves are shown in Fig. 3.7a. They show a single peak located at the Rabi frequency (already known from the time-domain measurements), without any harmonics within the 50 MHz detection window, as expected from theoretical predictions [53]. To be more quantitative, the measured $S(\omega)$ is converted into spin units, using a conversion factor $\delta V^2 = \delta I^2 + \delta Q^2$ measured as accurately as possible in a separate experiment by saturating the qubit transition [7, 8].

The resulting spin spectrum $\tilde{S}_z(\omega)$ is shown in Fig. 3.7b and is in good agreement with theoretical predictions. The data clearly show the transition from weak to strong measurement in a continuously monitored driven TLS : at low $\bar{n}$ the spectrum consists of a single Lorentzian peak at Ω_R; on increasing the measurement strength, this Lorentzian broadens towards low frequencies, and for strong measurements the spectrum becomes a Lorentzian centered at zero frequency, similar to that of an incoherent TLS jumping stochastically between its two states[53, 52]. The theoretical curves shown in Fig. 3.7c-f are obtained without adjustable parameter, using an analytical formula derived from the solution of Bloch equations in which the finite

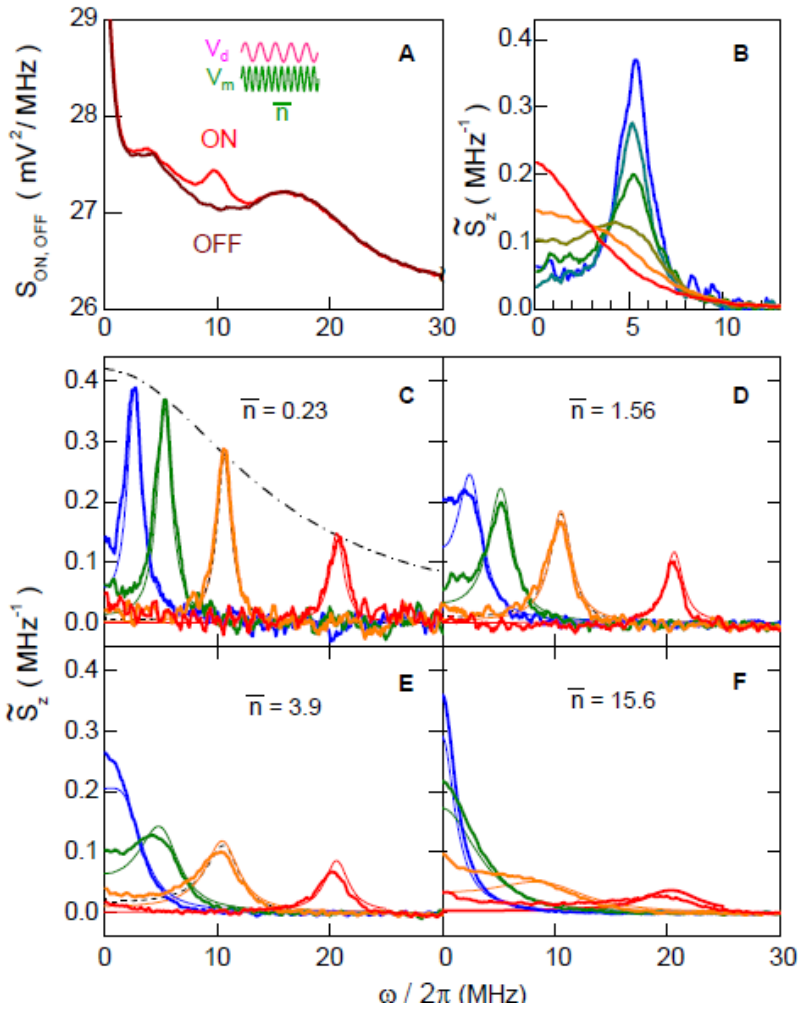

Figure 3.7: Continuous monitoring of the driven TLS. (a) Spectral densities $S_{ON}(\omega)$ and $S_{OFF}(\omega)$ when V_d and V_m are both OFF (brown) or both ON (red), with $\Omega_R = 2\pi 10$ MHz and $\bar{n} = 1$. The difference between the two curves shows the Rabi peak. (b) Normalized Rabi spectra at $\Omega_R = 2\pi 5$ MHz and $\bar{n} = 0.23, 0.78, 1.56, 3.9, 7.8,$ and15.6 (from blue to red). (C-F) Normalized Rabi peaks at $\omega_R/2\pi = 2.5, 5, 10 and 20$ MHz (from blue to red) for $\bar{n} = 0.23(C), 1.56(D), 3.9(E), and 15.6$ (F). Thick and thin color lines are respectively the experimental spectra and those calculated from a theoretical analytical formula using only independently measured parameters (including $\chi/2\pi = 1.8$ MHz). Dashed black lines on top of the orange curves in (C,D,E) are Rabi peaks obtained by numerical simulation with the same parameters. The dotted-dashed black curve in C is the Lorentzian frequency response $C(\omega)$ of the resonator.

detector bandwidth is taken into account phenomenologically. The agreement between theory and experiment is good for $\bar{n} \leq 5$ but is only qualitative at larger $\bar{n}$, possibly because of a breakdown of the dispersive approximation.

3.2.5 Experimental test of the Leggett-Garg inequality

Macrorealism

In the quantum trajectory description, the observation of the Rabi peak is possible because of the progressive and continuous projection of the qubit quantum state

towards eigenstates of σ_z caused by the measurement quantum back-action. However one could wonder whether an alternative model could yield the same curves. For instance, a "classical" variable such as the collective magnetization of a collection of spin-1/2, driven and continuously measured, would also yield a peak at the Rabi frequency, because even though the phase of the Rabi oscillation is lost after the transient nutation, this nutation continues and would have a spectral signature similar to the one oberved in Fig. 3.7. Quite remarkably, it is nevertheless possible to discriminate between a Rabi peak originating from a "classical" or from a quantum spin, as noticed by Ruskov and Korotkov [54]: indeed the amplitude of the Rabi peak for a quantum TLS should be slightly larger than the amplitude of any Rabi peak allowed for a "classical" system, as demonstrated below using a reasoning which is a weak measurement version of an earlier reasoning of Leggett and Garg [45].

Before presenting the original Leggett-Garg argument [45] it is necessary to be more precise about the meaning of the word "classical". In [45] Leggett and Garg consider systems satisfying two assumptions corresponding to a type of behavior that they call "macrorealism" : (A1) the system is always in one of its macroscopically distinguishable states and (A2) this state can be measured in a non-invasive way, that is without perturbing the subsequent dynamics of the system. Quantum mechanics however contradicts both assumptions, since a system can be in a superposition of any states, and any measurement in quantum mechanics has an unavoidable back-action. The macrorealistic assumptions are particularly plausible for systems that can be qualified of being "macroscopic". The example considered in the initial Leggett-Garg article is in fact precisely a superconducting SQUID being in two of its metastable flux-states - in fact a flux-qubit. It was therefore particularly relevant to test the validity of these two hypotheses on a superconducting qubit, even if its macroscopic character is subject to discussion and debate.

Leggett-Garg inequality with projective measurements

To obtain a quantitative test discriminating if a physical system obeys or not the two rather general assumptions (A1) and (A2), Leggett and Garg consider a certain degree of freedom, described by a variable $z(t)$ such that $-1 \leq z(t) \leq 1$, and fulfilling the macrorealistic axioms. Using a simple arithmetic argument in the spirit of the Bell inequalities, it is possible to show that unavoidably

$$z(t_0)z(t_1) + z(t_1)z(t_2) - z(t_0)z(t_2) \leq 1 \tag{3.4}$$

for all t_i. Consequently, an oberver measuring z on many identical systems, at t_0 and $t_1 = t_0 + \tau$, at t_0 and $t_2 = t_0 + 2\tau$, or at t_1 and t_2, should find ensemble-averaged correlators $K_{ij}(t_0, \tau) = \langle z(t_i)z(t_j)\rangle$ (for $i, j = 0, 1, 2$, with $i < j$) satisfying the Leggett-Garg inequality

$$f_{LG}(t_0, \tau) \equiv K_{01} + K_{12} - K_{02} \leq 1. \tag{3.5}$$

Quantum mechanics on the other hand predicts that, applied to the case of a qubit undergoing coherent oscillations at frequency Ω_R, this inequality is violated for well-chosen values of τ, with maximal violation $f_{LG}(t_0, \tau = \pi/3\Omega_R) = 1.5$ independent of t_0. Note that the delay τ between the successive measurements has a role analogous to the angle between the measurement directions in the Bell inequality

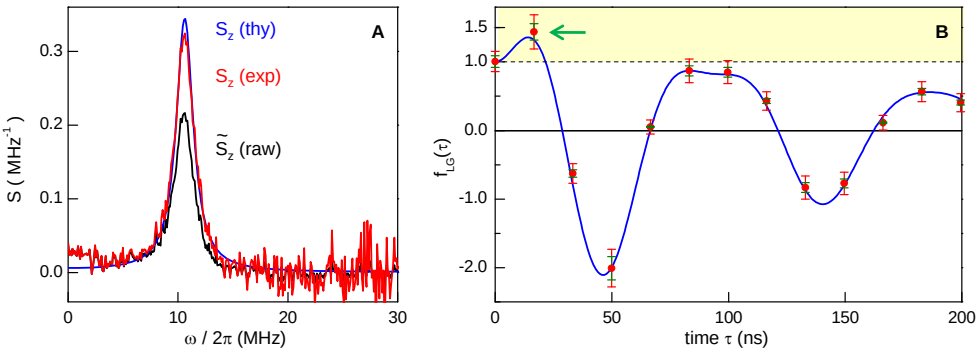

Figure 3.8: Experimental violation of the Leggett-Garg inequality. A) experimental (red) and theoretical (blue) spectral densities $S_z(\omega)$, calculated or measured at $\omega/2\pi = 10.6\,MHz$ and $\bar{n} = 0.78$. B) experimental (dots) and theoretical (blue line) Leggett-Garg function $f_{LG}(\tau) = 2K(\tau) - K(2\tau)$. Green error bars correspond to the maximum systematic error associated with calibration, whereas red ones also include a two standard deviation wide statistical error $\pm 2\sigma(\tau)$ associated with the experimental noise on $\tilde{S}_z$. The Leggett-Garg inequality is violated (yellow region) at $\tau = 17\,ns$ (see green arrow) by 5σ.

argument, justifying the nickname "Bell inequality in time". The excess of correlations predicted by quantum mechanics, compared to the macrorealistic case, can be interpreted as resulting from the projection of the qubit state onto a σ_z eigenstate induced by the first measurement.

Leggett-Garg inequality with weak continuous measurements

As shown in [54] the very same conclusions also hold if the qubit undergoing coherent oscillations is continuously and weakly monitored along σ_z as in our experiment, with the system in its steady-state implying that the two-time correlation functions depend only on the time difference. The detector now delivers an output signal $V(t) = (\delta V/2)z(t) + \xi(t)$ proportional to $z(t)$ with some extra noise $\xi(t)$. Macrorealism implies that the qubit dynamics at time $t + \tau$ is unaffected by the detector noise at time t which mathematically implies that $\langle \xi(t)z(t+\tau)\rangle = 0$. The detector output correlation function $K(\tau) = \langle V(t)V(t+\tau)\rangle/(\delta V/2)^2$ is then simply equal to $\langle z(t)z(t+\tau)\rangle$. By averaging inequality 3.5 over t_0 in the steady-state, the Leggett-Garg inequality in time 3.5 becomes

$$f_{LG}(\tau) \equiv 2K(\tau) - K(2\tau) \leq 1, \tag{3.6}$$

and should be violated by a quantum TLS. The violation here is due to a continuous partial projection caused by the measurement during the TLS coherent evolution, which reinforces correlations between the detector output at successive times.

Experimental test of the Leggett-Garg inequality

Using one of the measurements of Rabi peaks described in the previous paragraph, it is straightforward to compute $K(\tau)$ (after normalizing the data to account for the cavity finite bandwidth [7]), and thus $f_{LG}(\tau)$. The results are shown in Fig. 3.8 for a Rabi peak at 10 MHz, and a measurement strength $\bar{n} = 0.78$. They are in

quantitative agreement with predictions taking into account the known decoherence times of the qubit. Importantly, we measure $f_{LG}(\tau = 17\text{ns} = \pi/3\Omega_R) = 1.44(\pm 0.12) \pm 2 \times (\sigma = 0.065)$, which violates inequality 3.6 by 5 standard deviations σ. This is a proof that, even for a vanishingly small measurement power of less than one microwave photon in the cavity, the quantum measurement back-action cannot be neglected, and has strong measurable consequences on the detector output correlation function; or alternatively that the state of the transmon qubit in the experiment cannot be described as a classical variable such as the position of the moon, following the image used by Einstein as related by H. Mooij [61]. Further evidence for the quantum behavior of superconducting circuits was brought in particular with the violation of the Bell inequality in a system of two coupled phase qubits [62].

This first test of the Leggett-Garg inequality was performed using continuous weak measurements on a driven superconducting qubit in its steady-state. Since then, other experiments were conducted to test this inequality, with different systems and different types of measurements (see [63] for a review on the subject). An interesting direction consists in making the non-invasive measurement assumption (A2) as plausible as possible from a macrorealistic viewpoint. This can be achieved with a detector able to measure only one of the two states, and which is therefore truly non-invasive in the eyes of a macrorealist when it gives a null result. Such "ideal negative result" measurements were used to test the Leggett-Garg inequality with phosphorus donors in silicon [64] and in related experiments with NV centers in diamond [65, 66]. Another research topic is the link between Leggett-Garg inequality violation and so-called strange weak values which was pointed out by Williams and Jordan [67] and experimentally demonstrated with optical photons [68] and with superconducting qubits [69].

3.2.6 Weak measurements : perspectives

After measuring the detector output power spectrum of a continuously monitored qubit as in our experiment, the next step would be to implement Korotkov's ideas of quantum feedback. The idea is to use the information acquired in the course of a continuous measurement to actively feedback on the qubit drive and control fields, in order for instance to stabilize the phase of a Rabi oscillations so that it lasts forever. The only obstacle that prevented us from realizing this experiment is that the qubit signal represents only a small fraction of the detector output, because the cryogenic amplifier adds a large amount of noise to the qubit readout signal. More recently, several groups developed better amplifiers, with noise properties much closer to the quantum limit, which added little or even no noise in addition to the qubit signal. This has enabled a new generation of experiments on weak measurements which built upon our results [7]. Noticeable recent results are the stabilization of a Rabi oscillation by quantum feedback [57, 58], and very recently even the direct observation of quantum trajectories [70].

Chapter 4

Hybrid Quantum Circuits

In parallel to research on circuit QED with transmon qubits, I started developing a new research project in 2009, which occupied me progressively more and more since then and at present constitutes my main research direction. It consists in developing new "hybrid" quantum devices that combine superconducting quantum circuits and spins in crystals, and that will benefit from the interesting properties of each system : the strong coupling to electromagnetic fields and flexibility of the circuits, and the long coherence times of the spins.

The most straightforward way to harness these two complementary features is to use spins in crystals as storage medium for the quantum state of superconducting qubits. I will describe here in some detail two of the steps we made towards the implementation of such an operational spin-based quantum memory, namely the demonstration of strong coupling of a spin ensemble to a coplanar waveguide resonator, and the transfer of a quantum state from a qubit into this spin ensemble. The experiments were carried out by postdoc Yuimaru Kubo and PhD student Cécile Grezes, of whom I was the main supervisor; they strongly benefitted from collaborations with the group of Jean-Francois Roch and Vincent Jacques, who are the French experts of NV centers.

4.1 Hybrid Quantum Circuits

4.1.1 Rationale for the hybrid way

Quantum information processing protocols consist in more or less complex operations on abstract quantum states, and the choice of the system which should embody these states is left to the "quantum engineer": either microscopic systems such as atoms, ions, photons, electron and nuclear spins, or more macroscopic artificial systems such as superconducting qubits, nanomechanical resonators, semi-conducting heterostructures, ... Each of these physical implementations has specific advantages from the point of view of quantum information processing. Atoms and spins can have long coherence times because of their decoupling from the macroscopic environment; mechanical resonators can be functionalized; photons are interesting for communication; and superconducting circuits are well-suited for rapid entangling gates. It is then natural to imagine that the possibility of exchanging quantum states between all these different types of quantum systems will lead to new quantum devices with new functionalities. This is precisely the framework of the emerging field of Hybrid

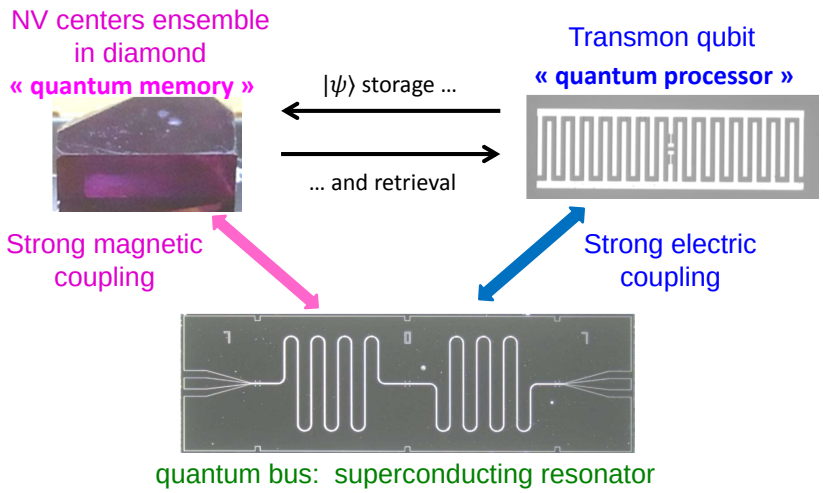

Figure 4.1: Spin-ensemble Quantum memory principle. The state $|\psi\rangle$ of a transmon qubit is stored into an ensemble of spins in a crystal, via an intermediate quantum bus consisting of a coplanar waveguide resonator coupled electrically to the qubit and magnetically to the spins.

Quantum Circuits.

The birth of this field is intimately linked to the development of circuit QED. Indeed, coplanar resonators offer a natural platform for coupling all kinds of quantum systems. Early proposals were motivated by the idea of increasing the coherence times of superconducting qubits, which was only on the microsecond scale at that time, while benefitting from their versatility and rapid single- and two-qubit gates. It was thus proposed to couple superconducting qubits, via the CPW quantum bus, to ions [71], atoms [72, 73, 74] and polar molecules [75], electrons on helium [76], or ensembles of impurity spins [77, 78, 42].

Experimental progress has been slow, because combining two different quantum systems requires to develop new experimental techniques to make them compatible which is sometimes challenging. Besides the case of spin-ensemble hybrid circuits which is discussed below, noteworthy progress was made in coupling atoms [79, 80, 81] and semiconducting quantum dots [35, 82] to coplanar waveguide resonators, and nanomechanical resonators to superconducting resonators and qubits [83, 84].

4.1.2 Towards a spin-ensemble quantum memory for superconducting qubits

Our hybrid project consists in combining electronic spins on the one hand, which can have ultra-long coherence times when embedded in clean crystals (up to seconds or more), and superconducting quantum circuits on the other hand, in the goal of realizing a quantum memory for superconducting qubits. We chose to use NV centers in diamond for their interesting properties and demonstrated long coherence times [85, 86]. The general goal of the experiment is to store the quantum state of a superconducting qubit into a NV centers ensemble quantum memory.

As schematically shown in Fig. 4.1, in our project the transmon qubit transfers its quantum state to the spin ensemble via an intermediate "quantum bus" resonator, to which the transmon is electrically coupled, and the spin ensemble magnetically

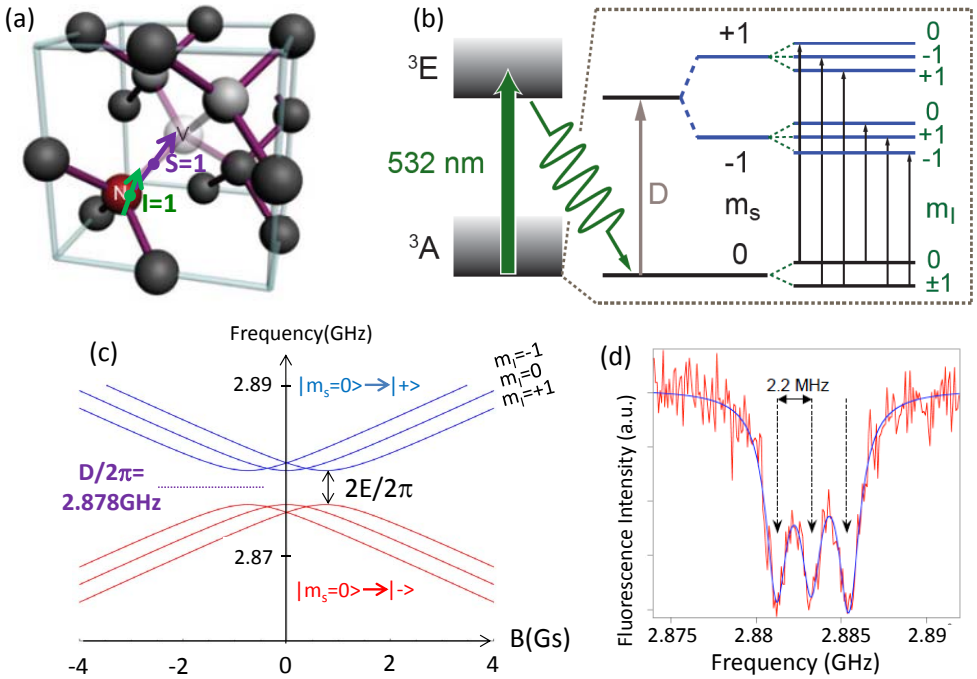

Figure 4.2: NV centers in diamond. (a) Negatively-charged NV centers consist of a substitutional Nitrogen atom next to a Vacancy of the diamond lattice, having trapped an electron. The electronic spin $S = 1$ is coupled to the $I = 1$ nuclear spin of the nitrogen atom by hyperfine interaction. (b) NV centers can be excited optically in an excited orbital state, through which they are repumped into the $m_S = 0$ state. (c) Transition frequency from the spin ground state $|m_S = 0, m_I\rangle$ to the excited states $|\pm, m_I\rangle$. (d) Optically-Detected Magnetic Resonance (ODMR) hyperfine spectrum of an ensemble of NV centers in a diamond crystal used for the experiment reported in paragraph 4.4 and [15].

coupled. This requires that the resonator is strongly coupled to the qubit, which is straightforwardly achieved with usual circuit QED techniques as described in the previous chapter, but also to the spin ensemble, which is more demanding and had never been achieved before.

4.2 Spin-ensemble quantum memory for superconducting qubits : principle

4.2.1 NV centers in diamond

NV centers are diamond defects consisting of a substitutional nitrogen atom (N) sitting next to a vacancy (V) of the diamond lattice (see Fig. 4.2a). In their negatively-charged state (NV^-), NV centers have very interesting electronic properties arising from their peculiar energy level scheme, shown schematically in Fig. 4.2b.

First, the electronic ground state of the NV is a spin-triplet $S = 1$, with a zero-field splitting $D/2\pi = 2.88\,\text{GHz}$ between states $m_S = \pm 1$ and $m_S = 0$ (along the NV center symmetry axis which plays the role of a natural quantization axis), arising because of spin-spin interactions in the diamond crystal field. The complete NV ground state spin Hamiltonian needs to be presented in some detail, since this is the degree of freedom that is used for storing the quantum information in our

experiments. Physically, four terms contribute to this Hamiltonian : (i) the zero-field splitting (ii) the Zeeman energy shift in an external magnetic field $\overrightarrow{B_{NV}}$ (iii) the interaction of the NV spin with local electric field or strain in the diamond due to the spin-orbit coupling, which causes the states $m_S = \pm 1$ to hybridize around zero magnetic field, and (iv) the hyperfine (HF) interaction of the NV electronic spin with the nuclear spin of the nitrogen atom, which is also a spin triplet $I = 1$ for the isotope ^{14}N used in our experiments. In total, the spin Hamiltonian [87] writes

$$H_{NV}/\hbar = DS_z^2 + \gamma_e \overrightarrow{B_{NV}} \cdot \overrightarrow{S} + E(S_x^2 - S_y^2) + A_z S_z I_z + Q[I_z^2 - I(I+1)/3], \quad (4.1)$$

with $S_{x,y,z}$ (resp. $I_{x,y,z}$) the spin angular momentum operators of the NV electron (resp. nitrogen nucleus), E the coupling induced by local strain and electric fields, $A_z/2\pi = -2.1\,\mathrm{MHz}$, $\gamma_e/2\pi = -28\,\mathrm{GHz/T}$ the electronic gyromagnetic ratio, and $Q/2\pi = -5\,\mathrm{MHz}$ the quadrupolar momentum of the nitrogen nuclear spin. The resulting energy levels are shown schematically in Fig. 4.2b. Only transitions between levels with the same nuclear spin state m_I are allowed, and their frequency from the ground state $|m_S = 0, m_I\rangle$ to $|\pm, m_I\rangle$ is shown in Fig. 4.2c in the case where $E/2\pi = 2\,\mathrm{MHz}$. Note that because of the spin-orbit term, the energy eigenstates $|\pm\rangle$ correspond to the pure spin states $m_S = \pm 1$ only for large magnetic fields, and are linear combinations of these spin states around zero magnetic field. From Fig. 4.2c one sees that superconducting circuits with resonance frequencies around 2.9 GHz can be brought into resonance with one of these spin transitions in a small magnetic field of a few Gauss, which is important since superconducting circuits have increased dissipation in large magnetic fields due to penetration of the film by vortices.

Another aspect is the optical properties of NV centers. Indeed, NV centers are optically active : when excited with green light, they fluoresce in the red. This is due to their excited electronic state (see Fig. 4.2b), which is also a spin-triplet. Ground-state to excited state transitions conserve the electronic spin; however the NV relaxation trom its excited state is spin-dependent: the $m_S = \pm 1$ state has a large probability of relaxing via a singlet metastable state (not shown in the energy diagram of Fig. 4.2b) which then relaxes to $m_S = 0$ in the ground state. After a few optical cycles, the NV center spin state is therefore repumped in $m_S = 0$ with a $\sim 90\%$ efficiency [88]. Since the metastable state is long-lived, the fluorescence intensity is reduced if the NV spin is initially in $m_S = \pm 1$ compared to $m_S = 0$. These remarkable properties enable the optical detection of the spin state of indivudal NV centers (so-called Optical Detection of Magnetic Resonance ODMR) at room-temperature, using a straightforward confocal microscope setup. For instance the spectroscopy of an ensemble of NV centers, measured at room-temperature by ODMR on one of our diamond samples, is shown in Fig. 4.2d. It displays the typical hyperfine structure of the ^{14}NV center transitions with a triplet of lines separated by 2.17 MHz. Numerous research groups worldwide use ODMR of individual NV centers to develop quantum information [89, 90] and magnetometry [91]. This is in particular the case in the group of Jean-Francois Roch and Vincent Jacques at ENS Cachan[92, 93], with whom we developed a fruitful collaboration which made possible the experiments reported here.

4.2.2 Coherence properties of NV centers

The interest of using NV centers for storing quantum information comes from the fact that long coherence times have been observed on the ground state spin transition in ultra-pure crystals. The coherence properties of NV centers are thus of utter importance for our project.

At room-temperature, the NV energy relaxation time is of order 5 ms, limited by the coupling to phonons, and is strongly enhanced at lower temperatures. Coherence properties are characterized by the Free-Induction Decay time T_2^* (measured by Ramsey fringes), the Hahn-echo decay time T_2 (measured by a spin-echo sequence), and the coherence time under dynamical decoupling sequences such as Carr-Purcell-Meiboom-Gil T_{2CPMG}. It is well-established that the values found for all these times depend crucially on the local magnetic environment of each NV center (in a sphere of few tens of nanometers diameter). In diamond, the main magnetic impurities surrounding the NVs are either neutral nitrogen atoms (so-called $P1$ centers) which have an electronic spin 1/2, or carbon 13 nuclei present to 1.1% abundance in natural carbon and which are nuclear spin 1/2. The longest coherence times were therefore measured in ultra-pure samples grown by Chemical-Vapor Deposition (CVD) with very low nitrogen concentration as well as an isotopically enriched carbon source. In such samples, $T_2^* = 500\mu$s [94] and $T_2 = 2$ ms [85] have been measured at room-temperature; at lower temperatures (100 K), $T_{2CPMG} = 0.5$ s was reached [86].

The crystals used in our experiments are however not as pure. Indeed, we need relatively large concentrations of NV centers of order $\sim 1 - 10$ ppm to efficiently absorb the microwave radiation. These concentrations are not easily reached with samples grown by CVD; our crystals instead are grown by another method called High-Pressure-High-Temperature (HPHT). HPHT diamonds usually have a large nitrogen concentration of $1 - 100$ ppm. To create NV centers the crystals are irradiated (either with protons or electrons) to create vacancies in the lattice; they are then annealed at $800 - 1000\,^{\circ}$C for few hours so that the vacancies migrate and form NV centers when they meet a nitrogen atom. This method unavoidably leaves a significant residual concentration of P1 centers ($1 - 100$ ppm), which limits the spin coherence time (both T_2^* and T_2) to lower values than reported above. In the experiments discussed here these residual P1 centers are the main cause of decoherence of the NV centers.

4.2.3 Coupling NV centers to a superconducting resonator

The coupling constant of a single NV to a resonator

To perform circuit QED experiments with NV centers, one needs to evaluate the interaction strength of a single NV center at position $\overrightarrow{r}$ coupled to the electromagnetic field in a CPW resonator via the magnetic dipole interaction. The coupling Hamiltonian is $H = -\overrightarrow{M} \cdot \overrightarrow{B}$, with $\overrightarrow{M} = \gamma_e \overrightarrow{S}$ and $\overrightarrow{B} = \overrightarrow{\delta B_0}(a + a^\dagger)$, $\overrightarrow{\delta B_0}(\overrightarrow{r})$ being the rms vacuum fluctuations of the magnetic field in the CPW resonator mode at $\overrightarrow{r}$. Restricting this Hamiltonian to one of the NV transitions (for instance the $m_S = 0 \rightarrow m_S = +1$ transition[1]), it can be rewritten in a Jaynes-Cummings form

[1] We suppose here to be in the high field limit where the energy eigenstates correspond to the pure spin states

$$H = \hbar g(\sigma_+ a + \sigma_- a^\dagger) \tag{4.2}$$

with $\hbar g = \gamma_e \langle m_S = +1| \overrightarrow{S} |m_S = 0\rangle \cdot \overrightarrow{\delta H_0}(\overrightarrow{r})$. If $\theta(\overrightarrow{r})$ is the angle between the NV axis and the microwave field, choosing z as the NV axis and x as the orthogonal direction in the $(z, \delta B_0(\overrightarrow{r}))$ plane, one finds $\hbar g = \gamma_e |\langle m_S = +1|S_x|m_S = 0\rangle||\delta B_0(\overrightarrow{r})|| \sin\theta(\overrightarrow{r})|$, yielding

$$g = \gamma_e |\delta B_0(\overrightarrow{r})|| \sin\theta(\overrightarrow{r})|/\sqrt{2}, \tag{4.3}$$

since $\langle m_S = +1|S_x|m_S = 0\rangle = \hbar/\sqrt{2}$. The coupling constant is thus governed by the amplitude of the vacuum field fluctuations at the spin location $|\delta B_0(\overrightarrow{r})|$. For a conventional CPW resonator as frequently used in circuit QED (with transverse dimensions of order 10μm and a 50Ω characteristic impedance), one finds $|\delta B_0(\overrightarrow{r})| \approx 4\mu$Gs, which gives a coupling constant $g/2\pi \approx 10\,$Hz for $\theta(\overrightarrow{r}) = \pi/2$. This is many orders of magnitude too low to reach the strong coupling regime, since the highest-Q CPW resonators reported so far have $Q = 10^6$ and therefore a 3 kHz linewidth at the NV frequency of 3 GHz.

Collective coupling

To make the coupling stronger, our approach is to use a large ensemble of N spins instead of a single one, each located at a position $\overrightarrow{r_j}$ and coupled to the cavity field with a constant $g_j(\overrightarrow{r_j})$. The coupling Hamiltonian then writes

$$H_{ens} = a \sum g_j(\overrightarrow{r_j})\sigma_{+,j} + a^\dagger \sum g_j^*(\overrightarrow{r_j})\sigma_{-,j}, \tag{4.4}$$

indicating that excitations in the resonator mode are coupled to a well-defined coherent superposition of spin excitations (analogous to a spin-wave). In the limit where the number of system excitations is small compared to N, this spin-wave behaves as a harmonic oscillator described by an annihilation operator $b = \sum(g_j(\overrightarrow{r_j})/g_{ens})\sigma_{-,j}$, with $g_{ens} = \sqrt{\sum |g_j|^2}$. Indeed, the commutator

$$\begin{aligned} [b, b^\dagger] &= \sum |g_j|^2 [\sigma_{-,j}, \sigma_{+,j}] && (4.5)\\ &= (\sum |g_j|^2 \sigma_{z,j})/g_{ens}^2 && (4.6)\\ &\approx 1, && (4.7) \end{aligned}$$

since in the limit of small excitation numbers, the mean excitation of each spin is $\ll 1$ and one can therefore approximate $\sigma_{z,j} \approx 1$. Using the collective operator b the coupling Hamiltonian is rewritten as

$$H_{ens} = g_{ens}(ab^\dagger + a^\dagger b). \tag{4.8}$$

The field is thus coupled to the collective spin operator b with a coupling strength g_{ens} which scales like $\sqrt{N}$, implying that with 10^{12} spins the ensemble coupling constant can reach $g_{ens}/2\pi \approx 10\,$MHz, largely sufficient to reach the strong coupling condition this time. This collective enhancement of the coupling constant is well known in atomic physics and was demonstrated in several experiments [95, 96, 97]; it can be qualitatively understood by the simple fact that at short times, one photon

present in the cavity has a probability N times larger to be absorbed by N spins in a given time than by a single spin.

The collective mode b is called the super-radiant mode, by opposition to $N-1$ other collective spin modes that are not coupled to the radiation field and which are called dark modes. An elementary excitation of this collective mode is described by a massively entangled state of all N spins called a Dicke state

$$b^\dagger|0_1...0_N\rangle = (g_1|1_1...0_N\rangle + ... + g_N|0_1...1_N\rangle)/g_{ens}. \tag{4.9}$$

Inhomogeneity issues

One noteworthy issue makes the situation slightly more complex than described in the previous paragraph: the frequency spread of all the NV centers in the sample. Indeed, as mentioned earlier each NV has a slightly different magnetic local environment due to the specific and random distribution of paramagnetic impurities in its close vicinity (the typical relevant scale being $\approx 10\,\mathrm{nm}$) and therefore its own resonance frequency ω_j, a phenomenon known as inhomogeneous broadening of the spin resonance. This leads to a more complex situation than the usual Tavis-Cummings model of atomic physics described just above. Indeed the Dicke state $(g_1|1_1...0_N\rangle + ... + g_N|0_1...1_N\rangle)/g_{ens}$ in which an excitation from the cavity can be stored is no longer stationary since each spin state will acquire a different relative phase $\phi_i = \omega_i\tau$ after a delay τ, turning the collective state into $(g_1|1_1...0_N\rangle \exp^{-i\phi_1} +... + g_N|0_1...1_N\rangle \exp^{-i\phi_N})/g_{ens}$ whose overlap with the initial super-radiant state decays rapidly with τ. With the help of A. Auffeves and I. Diniz we analyzed this problem theoretically [98], in parallel with Z. Kurucz and K. Moelmer in Aarhus [99].

To obtain a more precise understanding of the effect of inhomogeneous broadening, we write the total system Hamiltonian

$$H/\hbar = \sum -\frac{\omega_j}{2}\sigma_{z,j} + \omega_c a^\dagger a + g_{ens}(ab^\dagger + a^\dagger b) \tag{4.10}$$

and compute the Heisenberg equations of motion for the field operator

$$\dot{a} = -i\omega_c a - ig_{ens}b \tag{4.11}$$

and for the super-radiant mode

$$\begin{aligned} \dot{b} &= i[\sum -\frac{\omega_j}{2}\sigma_{z,j}, \sum \frac{g_k}{g_{ens}}\sigma_{-,k}] - ig_{ens}a & (4.12)\\ &= -i\sum \frac{\omega_j g_j}{g_{ens}}\sigma_{-,j} - ig_{ens}a. & (4.13) \end{aligned}$$

If we then define the mean NV frequency $\bar{\omega} \equiv \sum |g_j/g_{ens}|^2\omega_j$ and the spin frequency variance $\Delta\omega^2 \equiv \sum |\omega_j - \bar{\omega}|^2|g_j/g_{ens}|^2$, this last equation can be rewritten as

$$\dot{b} = -i\bar{\omega}b - ig_{ens}a - i\Delta\omega c, \tag{4.14}$$

where $c = (\Delta\omega)^{-1}\sum(\omega_j - \bar{\omega})(g_j/g_{ens})\sigma_{-,j}$ is a collective spin operator not directly coupled to the resonator mode (i.e. one of the "dark modes"). This mode is

orthogonal to b since $[c, b^\dagger] = 0$. Equations 4.11 and 4.14 show that if all the spins had the same frequency (case $\Delta\omega = 0$), a and b would form a closed system, rigorously decoupled from all other dark modes. An excitation initially present in the cavity would therefore be absorbed and re-emitted coherently by the super-radiant spin mode, at a frequency g_{ens}. However in the presence of non-zero inhomogeneous broadening, the super-radiant mode b is no longer stationary; it is instead coupled with a strength $\Delta\omega$ to the dark mode c, which is itself coupled to another dark mode, and so forth. Since there are many ($N - 1$, with $N \approx 10^{11}$) dark modes, one can expect that the excitation initially exchanged coherently between modes a and b eventually decays into this "bath" of dark modes, in a time of order $\Delta\omega^{-1}$ which is precisely the Free-Induction-Decay time of the ensemble T_2^*.

It is worth stressing that the issue here is the inhomogeneity of the NV frequencies. The spread of the NV coupling constants to the cavity mode throughout the ensemble is on the contrary not detrimental to the storage of a quantum state as we envision it here.

The analysis above allows us to establish a new strong-coupling criterion for the case of a cavity mode coupled with N inhomogeneously broadened spins: in the limit where

$$g_{ens} > \kappa, \Delta\omega \tag{4.15}$$

the cavity mode and the superradiant spin mode can exchange excitations coherently several times before they leak out into the bath of dark states or outside of the cavity. In this strong coupling limit the system spectrum should show well-resolved polaritonic peaks separated by $2g_{ens}$ when the cavity and spins are tuned into resonance.

4.2.4 Input-Output theory

Even though the above argument enables to qualitatively understand the effect of inhomogeneous broadening, we haven't explained here how to compute actual physical quantities such as the transmission spectrum of a resonator coupled to a spin ensemble, or the dynamics of this coupled system. Using input-output theory it is possible to do so as described in [98, 99]; in this way quantitative theoretical predictions can be made as seen in the following, provided the spin density function $\rho(\omega) = \sum \delta(\omega - \omega_j)$ (which can be determined by ODMR) is known.

4.3 Strong coupling of an ensemble of NV centers to a resonator

Our first experimental result [14] was the spectroscopic evidence for strong coupling between an ensemble of NV centers and a frequency-tunable superconducting resonator.

4.3.1 Experimental setup

The experiment is sketched in Fig. 4.3(a,b,c). A diamond crystal ($3 \times 3 \times 0.5\text{mm}^3$) containing the NV centers is glued with vacuum grease on top of a half-wavelength

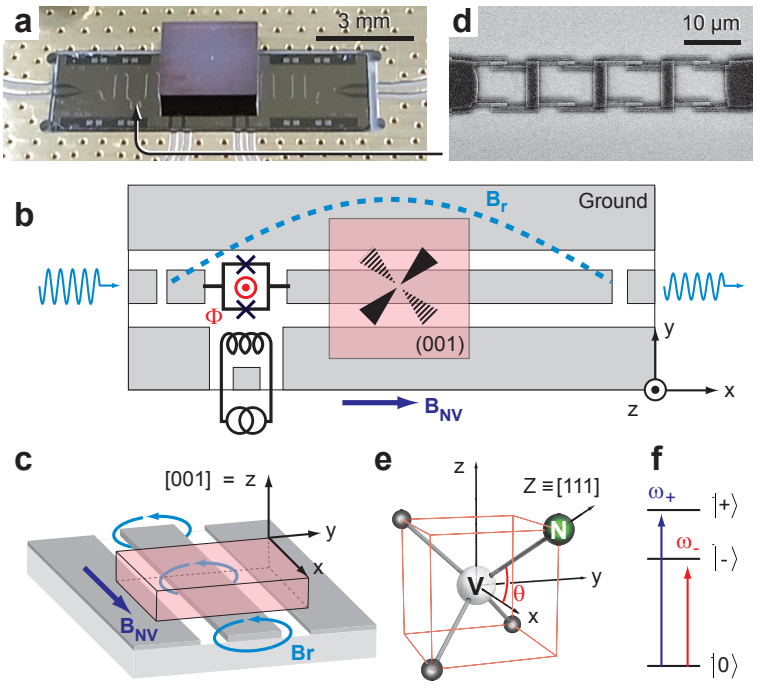

Figure 4.3: Strong coupling between NVs and a superconducting resonator : Experimental setup. (a) Photograph of the chip with diamond sample glued on top. (b,c,e,f) Equivalent electrical circuit. The coplanar resonator frequency ω_r can be tuned with the flux Φ applied through the SQUID loop via an on-chip line. The resonator transmission coefficient is measured. Due to the diamond crystalline orientation with respect to the applied magnetic field B_{NV}, the 4 NV center families undergo the same Zeeman shift and have degenerate transition frequencies ω_- and ω_+. (d) Electron micrograph of the 4-SQUID array (extracted from [14]).

niobium coplanar waveguide resonator, with a distance to the silicon substrate less than $\approx 0.5\mu$m to ensure a maxium spin-resonator coupling. The diamond is positioned in the middle of the resonator where the magnetic field is maximum, with its (001) crystallographic plane facing the chip. The spin Zeeman splitting can be tuned with a magnetic field $\overrightarrow{B_{NV}}$ parallel to the sample surface along the [100] axis within a few degrees.

An array of four SQUIDs (see Fig. 4.3d) was inserted in the resonator central conductor, away from the diamond crystal, to make its frequency $\omega_r(\Phi_x)$ tunable with the magnetic flux Φ_x threading the SQUID loops [100]. This flux is generated by passing current through an on-chip wire so that the resonator can be brought in resonance with the spins without changing their Zeeman splitting. The resonator transmission $S_{21}(\omega)$ is measured with a network analyzer, at powers low enough for the current through the SQUIDs to stay well below their critical current so that the resonator behaves linearly.

4.3.2 Sample characterization

The coplanar resonator and diamond crystal were first characterized separately. The transmission amplitude of the resonator cooled at 40 mK and at $\Phi_x = 0$, is shown in Fig. 4.4a. Its frequency dependence with Φ_x is in good agreement with predictions [100] (see Fig. 4.4b).

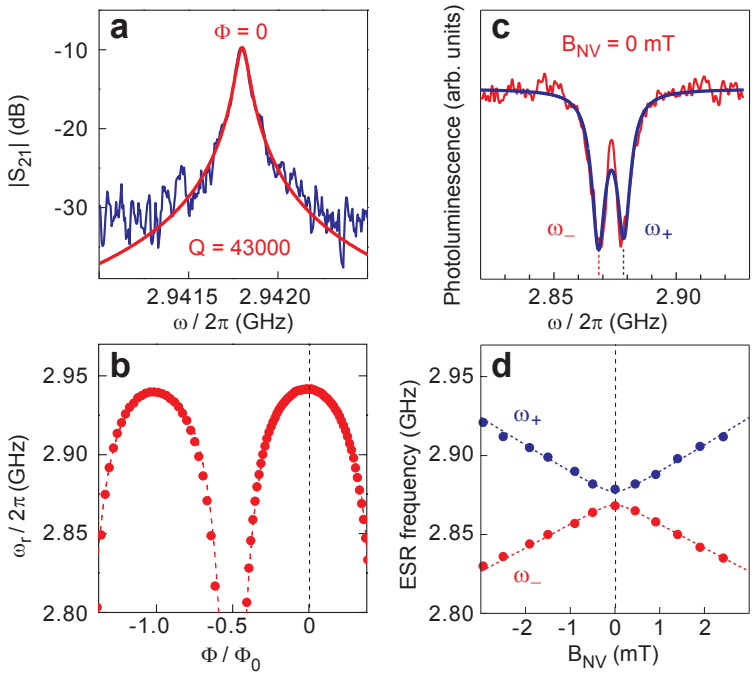

Figure 4.4: Sample characterization. (a) Tunable resonator transmission (at 40 mK) for $\Phi = 0$ with Lorentzian fit (red curve), showing a resonance with $Q = 4 \cdot 10^4$. (b) Measured (full circles) and predicted (dashed red line) resonator frequency dependence $\omega_r(\Phi)$. (c) Magnetic resonance spectrum (detected by ODMR at 300 K) of the NV ensemble used in the experiment, for $B_{NV} = 0$, showing the 2 resonance frequencies ω_- and ω_+. The blue line is a fit with a sum of two Lorentzians. (d) Measured (dots) and predicted (dotted lines) NV frequency dependence on B_{NV} for B_{NV} applied along the [100] *axis (extracted from [14]).*

The diamond crystal is of the HPHT type, with a nominal 100 ppm nitrogen concentration. After irradiation and annealing, we measured a NV concentration of $\approx 1.2 \cdot 10^6 \mu\text{m}^{-3}$ (that is, 7 ppm) by comparing the sample photoluminescence to the photoluminescence of an individual center in the same conditions. The NV spectrum at $B_{NV} = 0$ mT measured by ODMR is shown in Fig. 4.4c. It consists of two lines at frequencies ω_- and ω_+ due to the strain-induced splitting with $E/2\pi \approx 4$ MHz. The resonance frequencies vary as expected when applying a magnetic field along the [100] axis (see Fig. 4.4d); note that only two lines are observed because for this magnetic field orientation the frequencies of the 4 different NV axis orientations are degenerate. The measured linewidth is $\Delta\omega/2\pi \approx 6$ MHz, due to dipolar interactions with the residual P1 centers (with estimated concentration ~ 100 ppm).

4.3.3 Normal mode splitting

Measurements of the resonator transmission at 40 mK with the diamond crystal on top are shown in Fig. 4.5. Two-dimensional plots of the transmission spectrum as a function of Φ_x are presented for 3 values of B_{NV}. For each B_{NV} two avoided crossings are observed when the resonator is tuned through the NV center ESR frequencies, which reveal the strong coupling of the NV ensemble to the resonator. To model these results we use the 3-mode Hamiltonian $H/\hbar = \omega_r(\Phi_x)a^\dagger a + \tilde{\omega}_+ b_+^\dagger b_+ + \tilde{\omega}_- b_-^\dagger b_- + g_+(a^\dagger b_+ + h.c.) + g_-(a^\dagger b_- + h.c.)$, where we introduced two super-radiant

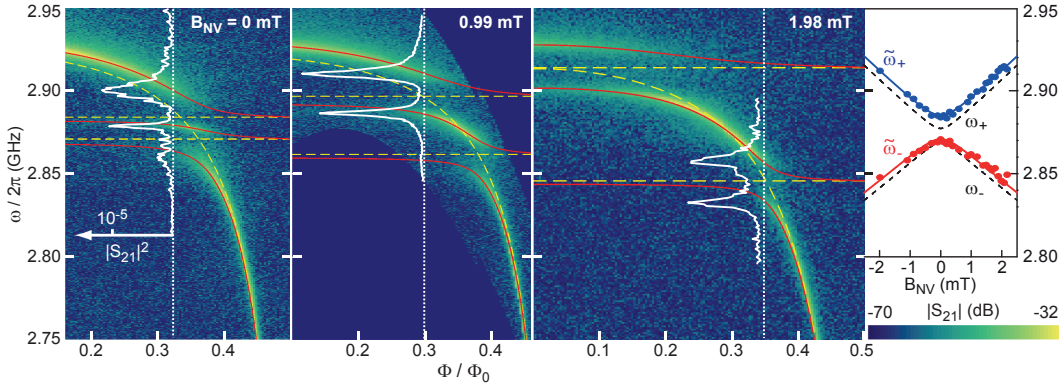

Figure 4.5: Tunable resonator transmission coefficient amplitude $|S_{21}|(\omega)$ as a function of Φ, for $B_{NV} = 0, 0.99, 1.98\,mT$. Each graph shows two avoided level crossing whenever $\omega_r(\Phi)$ crosses $\tilde{\omega_-}(B_{NV})$ and $\tilde{\omega_+}(B_{NV})$, the NV resonance frequencies at low temperatures. (right panel) Measured (dots) and predicted (solid curves) values of $\tilde{\omega_\pm}(B_{NV})$, together with the room-temperature values $\omega_\pm(B_{NV})$ (dashed line) (extracted from [14]).

spin modes $b_\pm$ for each ESR frequency $\tilde{\omega}_\pm$. The transmission spectrum was fitted for each Φ_x by a sum of Lorentzian peaks whose central frequencies are then fitted to the eigenfrequencies of H, yielding the red solid lines in Fig. 4.5. The $\tilde{\omega}_\pm(B_{NV})$ is well described by the NV center Hamiltonian, taking into account a slight change of the zero-field splitting and of the average strain in the crystal compared to the room-temperature values as seen in Fig. 4.5. The fitted coupling constants are $g_+/2\pi = g_-/2\pi = 11\,\text{MHz}$, indeed larger than the spin and resonator linewidths, which confirms that the strong coupling regime is indeed reached. They are in quantitative agreement with the values estimated from the measured NV center concentration.

Since these measurements, normal mode splittings between a spin ensemble and a superconducting resonator mode have been observed in several different experiments: again NV centers [101] and P1 centers [102] in diamond, and rare-earth ions in YSO [103].

4.4 Transfer of a qubit state into the NV ensemble

After the spectroscopic evidence for strong coupling between an ensemble of NVs and a resonator, the next step was to add a superconducting qubit on the chip with its readout circuit and to demonstrate the transfer of its quantum state into the NV spin ensemble. For that it was essential to have a narrower NV resonance. Pr. Isoya from Tsukuba University provided us with a diamond crystal containing a lower concentration of P1 centers while still being sufficiently doped in NV centers for our experiments.

4.4.1 Sample design and spectroscopy

A schematic picture of our experiment is shown in Fig. 4.6. We integrate on the same chip the diamond crystal containing the NV centers ensemble (denoted NV)

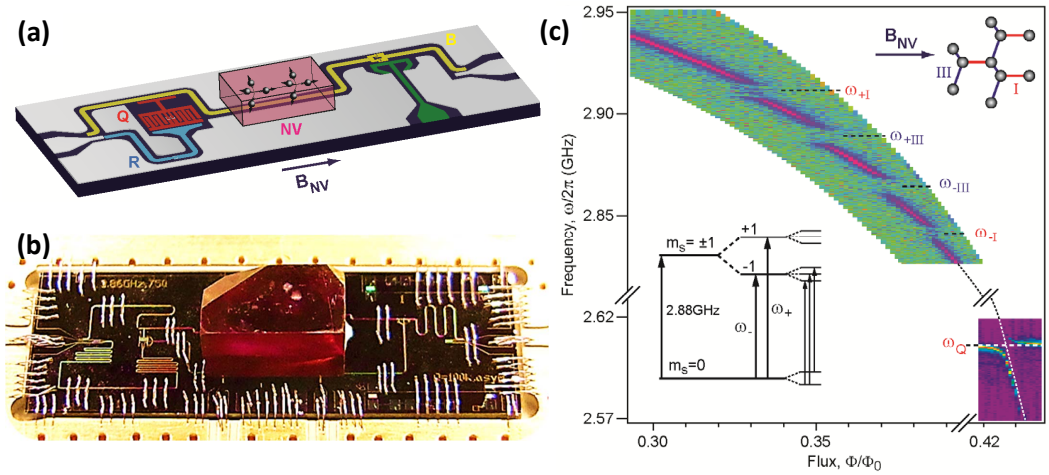

Figure 4.6: Single-photon storage: Sample layout. (a) Schematic view of the sample, including a diamond crystal with the NV ensemble NV, and a transmon qubit Q (in red). They are coupled via the quantum bus coplanar resonator B (in yellow) whose frequency can be adjusted by passing current in a flux line (in green). The qubit is driven and readout via the bistable resonator R (in blue). A magnetic field B_{NV} is applied parallel to the sample surface. (b) Photograph of the sample with diamond on top (the purple color is due to the NV centers). (c) Transmission coefficient amplitude $|S_{21}|$ of B, showing 4 anticrossings corresponding to the 2 ESR frequencies $\omega_\pm$ of each of the 2 NV families I, III undergoing different Zeeman shift due to their crystalline orientation as shown in the right top inset. At lower frequency an anti-crossing with the transmon qubit is seen at $\omega_Q/2\pi = 2.607$ GHz (extracted from [15]).

and a transmon qubit Q (with transition frequency ω_Q between its levels $|g\rangle$ and $|e\rangle$). Their interaction is mediated by a quantum bus: a coplanar resonator B whose frequency ω_B can be tuned on a nanosecond timescale by changing the flux Φ through the loop of a SQUID integrated in the resonator central conductor. The qubit is driven and readout through a second dedicated resonator R, using standard circuit QED methods. Note that contrary to the experiments described in the previous chapter, R was made non-linear by inserting a Josephson junction in its middle, which transforms the resonator into a high-fidelity sample-and-hold detector of the qubit state [11] enabling a direct measurement of the qubit excited state probability P_e.

The diamond is a HPHT crystal with 40 ppm initial nitrogen concentration (i.e. P1 centers). After irradiation and annealing, the NV concentration measured by photoluminescence is 2.5 ppm, implying a probable final P1 concentration of 35 ppm, i.e. $3-4$ times lower than in the experiment reported in paragraph 4.3. As a result, the NV linewidth is also narrower, as can be seen from the ODMR spectrum shown in Fig. 4.2 which was measured on this sample, where the hyperfine NV structure is well-resolved with a linewidth of ≈ 1.5 MHz for each peak.

As in the previous experiment, the diamond crystal is glued on top of the resonator with vacuum grease. The degeneracy between states $|\pm\rangle$ is lifted with a $B_{NV} = 1.1$ mT magnetic field applied parallel to the chip and along the $[1,1,1]$ crystalline axis [2]. The NV frequencies being sensitive only to the projection of B_{NV} along the $N-V$ axis, two groups of NVs thus experience different Zeeman effects:

[2] note that B_{NV} is wrongly mentioned to be 1.4 mT in the original article [15, 16]

those along $[1,1,1]$ (denoted I) and those along either of the three other $\langle 1,1,1\rangle$ axes (denoted III as they are 3 times more numerous). This results in four different ESR frequencies $\omega_{\pm I,\pm III}$.

They are visible as 4 avoided crossings in the resonator transmission spectrum (see Fig. 4.6c) as a function of Φ, similar to the results reported in paragraph 4.3. From the data we also deduce the ensemble coupling constants $g_{\pm I}/2\pi = 2.9\,\mathrm{MHz}$ and $g_{\pm III}/2\pi = 3.8\,\mathrm{MHz}$, lower than in the results of paragraph 4.3 due to the lower NV concentration. At a frequency much lower than the 4 NV center ESR frequencies we observe another avoided crossing, this time due to the interaction with the transmon qubit. The transmission spectrum in Fig. 4.6c shows that the tunable resonator can be used as a bus to dynamically transfer excitations from the qubit into the NV ensemble at one of its resonance frequency.

4.4.2 Transfer of a superconducting qubit state into the NV ensemble

The pulse sequence used to transfer an arbitrary qubit state $|\psi\rangle$ into the spin ensemble is shown in Fig 4.7. The state is first transferred from the qubit into the bus resonator with an adiabatic SWAP gate (*aSWAP* operation), by adiabatically sweeping ω_B across ω_Q. B is then brought at a frequency $\omega_B(\Phi)$ in or near one of the spin ensemble resonances for a duration τ; the resulting B state is then transferred back into the qubit, which is finally read-out.

The result is shown in Fig. 4.7, for $\omega_B(\Phi) = \omega_{-I}$ and two different initial qubit states. For $|\psi\rangle = |e\rangle$ (see Fig. 4.7a), an oscillation of small amplitude in P_e is observed, revealing the storage in the spin ensemble of the single quantum of excitation initially in the qubit at $\tau_s = 97$ ns, and its retrieval back into the qubit at $\tau_r = 146$ ns. Similar results were obtained at the same time by a Japanese group at NTT Research Labs, with a NV ensemble directly coupled to a flux-qubit [43].

The fidelity of this storage-retrieval process, defined as $P_e(\tau_r)/P_e(0)$, is only of 0.07 for group I (it was twice larger for group III [15]). This relatively low value is not due to a short spin dephasing time, but rather to an interference effect caused by the HF structure of NV centers, as evidenced by the non-exponential damping observed in $P_e(\tau)$. The measurements are accurately reproduced by a full calculation of the spin-resonator dynamics [99, 98, 104] taking into account this HF structure, with the linewidth of each HF peak as the only adjustable parameter. A linewidth of 1.6 MHz (compatible with ODMR measurements shown in Fig. 4.2d) is in this way determined for the spins in group I.

A quantum memory should be able not only to store the qubit basis states, but also an arbitrary superposition with a well-defined phase. To demonstrate that, we repeated the experiment with $|\psi\rangle = (|g\rangle + |e\rangle)/\sqrt{2}$ as shown in Fig. 4.7b. Instead of measuring the qubit at the end of the sequence with a simple readout pulse yielding only the qubit $\langle\sigma_Z\rangle$, we perform a full quantum tomography of the qubit state to test in particular if the phase of the initial superposition state was preserved during the transfer to the spins. After substracting a trivial rotation around Z occurring at frequency $(\omega_{-I} - \omega_Q)$, we reconstruct the trajectory of this Bloch vector as a function of the interaction time τ. It is plotted in Fig. 4.7b, together with the off-diagonal element ρ_{ge} of the final qubit density matrix, which quantifies its coherence. We find that no coherence is left in the qubit at the end of the sequence

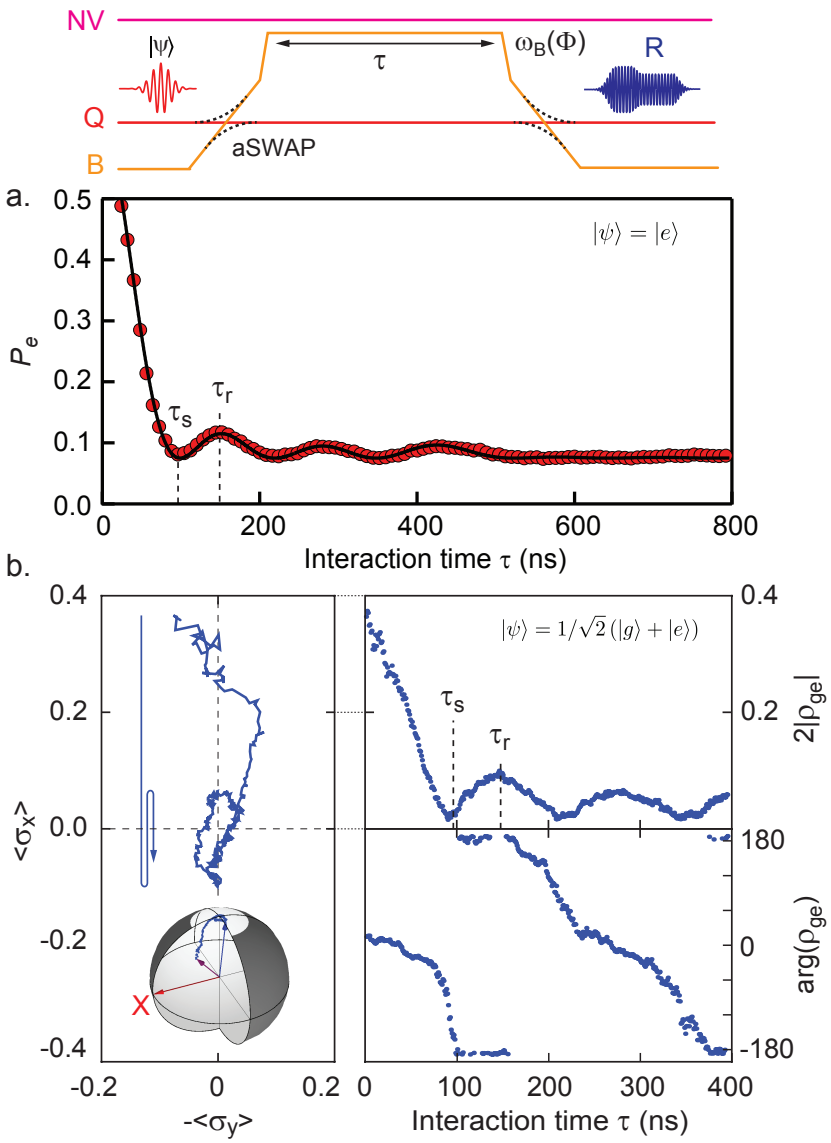

Figure 4.7: Transfer of a qubit state into the spin ensemble. (top) Pulse sequence. The qubit is prepared in state $|\psi\rangle$ with the appropriate pulse sequence; this state is then transferred to B by an adiabatic swap operation aSWAP; after which the bus is tuned near the spin resonance at frequency $\omega_B(\Phi)$ during a time τ; the final bus quantum state is transferred back to the qubit. The qubit state is either measured with a simple readout pulse yielding the excited state probability p_e, or with full quantum state tomography yielding the qubit $\langle\sigma_Z\rangle$, $\langle\sigma_X\rangle$, and $\langle\sigma_Y\rangle$. (a) Qubit excited state probability $p_e(\tau)$ for $\omega_B(\Phi) = \omega_{-I}$ and $|\psi\rangle = |e\rangle$. A single microwave photon is transferred into the spin ensemble at time τ_s and retrieved at time τ_r. (b) Qubit quantum state tomography for $\omega_B(\Phi) = \omega_{-I}$ and $|\psi\rangle = (|g\rangle + |e\rangle)/\sqrt{2}$. The left panel shows the trajectory of the qubit Bloch vector; the right panel shows the off-diagonal density matrix element ρ_{ge} which quantifies its coherence (extracted from [15]).

for $\tau = \tau_s$, as expected for a full storage of the initial state into the ensemble. Then, coherence is retrieved at $\tau = \tau_r$, although with an amplitude ~ 5 times smaller than its value at $\tau = 0$ (i.e. without interaction with the spins). Note the π phase shift occurring after each storage-retrieval cycle, characteristic of 2π rotations in the two-level space $\{|1_B, 0_{-I}\rangle, |0_B, 1_{-I}\rangle\}$. The combination of the results

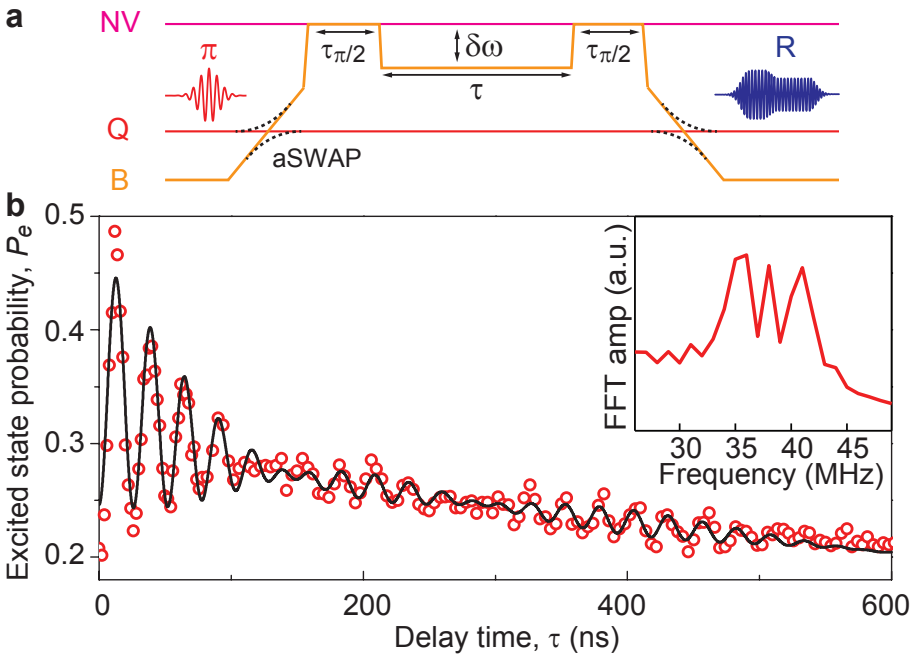

Figure 4.8: Evidence for entanglement between a resonator and a spin-ensemble. (a) Pulse sequence. The resonator is prepared in $|1_B\rangle$ state by transfer of the qubit excitation. It is then tuned in resonance with the NV ensemble at ω_{-I} for $\tau_{\pi/2} = \tau_{s,-I}/2$ generating an entangled state of the two systems. B is then detuned from the spins by $\delta\omega/2\pi = 38$ MHz during τ, after which a second half-swap is performed. The excitation remaining in B is then transferred back to the qubit which is finally readout. (b) Measured (red circles) and calculated (black line - see text) probability $P_e(\tau)$, as well as its Fourier transform (inset) revealing the NV centers HF structure (extracted from [15]).

of Figs. 4.7a and b demonstrates that arbitrary superpositions of the two qubit states can be stored and retrieved in a spin ensemble - although with limited fidelity - and thus represents a first proof-of-concept of a spin-based quantum memory for superconducting qubits [15].

4.4.3 Resonator-spin ensemble entanglement

Stopping the NV - bus swap interaction at half of the storage time τ_s yields an interesting situation where the single excitation is shared coherently between the spin ensemble and the quantum bus. This is described by the maximally entangled photon-spin state $|\psi_{BS}\rangle = (|1_B 0_s\rangle + |0_B 1_s\rangle)/\sqrt{2}$. One way to probe the quantum coherence of this state superposition is shown in Fig. 4.8: after preparing $|\psi_{BS}\rangle$, the resonator is suddenly detuned from the NV frequency by $\delta\omega$. After a time τ, $|\psi_{BS}\rangle$ should evolve into $(|1_B 0_s\rangle + \exp^{i\phi} |0_B 1_s\rangle)/\sqrt{2}$ with $\phi = \delta\omega\tau$; tuning back the resonator into resonance with the NV ensemble for a time $\tau_s/2$ then converts the phase ϕ into population of state $|1_B 0_s\rangle$. This population is transferred to the qubit, and readout.

Oscillations at frequency $\delta\omega$ are observed in $P_e(\tau)$ as seen in Fig. 4.8, confirming that the resonator and the spins are entangled after the first $\pi/2$ pulse. These oscillations are modulated by a beating pattern, with an overall damping of the oscillations envelope in $\sim$ 200 ns. Quite remarkably, this beating observed in the qubit excited state probability is directly caused by the HF structure of NV centers,

as proved by the Fourier transform of $P_e(\tau)$ which shows the three HF lines. The full calculation of the system dynamics quantitatively captures both the beatings and the oscillations damping, which is thus completely explained by the 1.6 MHz inhomogeneous linewidth of each HF line taken into account in the theory.

4.5 Towards an operational spin-ensemble quantum memory

The experiments reported above demonstrate the possibility of storing a qubit state into a spin ensemble. However they do not constitute an operational quantum memory since the storage time is only of order 100 ns, much shorter than present-day qubit coherence times. As explained earlier, due to inhomogeneous broadening in the NV ensemble, the quantum state decays into the bath of dark modes shortly after its transfer to the super-radiant mode. The challenge of an operational quantum memory is therefore to *retrieve* this state long after it has dephased, using dynamical decoupling methods such as spin-echoes or more complex sequences (CPMG or others).

This is the path in which we are engaged since 2012, and the PhD subject of C. Grezes. I will here only briefly describe the steps taken in that direction:

(i) Together with K. Moelmer and his postdoc B. Julsgaard, we have first designed a realistic proposal [105] for a quantum memory protocol that overcomes inhomogeneous broadening using adiabatic refocusing pulses applied to the spins, combined with dynamic tuning of the resonator frequency and quality factor. One key interest of this protocol is its capacity to store in parallel many qubit states, due to the large number of degrees of freedom in the spin ensemble. This multi-mode capability of the spin-ensemble quantum memory opens the exciting perspective to store in one single diamond crystal hundreds of (possibly entangled) qubit states. This clearly shows the major impact that an operational quantum memory of this type would have on qubit-based quantum information processing.

(ii) On the experimental level, we have made progress towards the implementation of this protocol by demonstrating the storage and retrieval with spin-echo of very weak microwave pulses (corresponding to $\approx 10^4$ photons in the cavity) [106], an encouraging indication that inhomogeneous broadening can indeed be overcome. Note that to obtain this result we had to implement optical repumping of the NVs inside our dilution cryostat [106].

With these technical steps recently taken, combined with samples of even higher quality provided by J. Isoya, the implementation of an operational quantum memory, able to store hundreds of qubit states for long times and to retrieve any of them on-demand, seems within reach.

Chapter 5

Conclusion and Perspectives

In this manuscript I have given an overview of the results obtained in quantum physics and quantum information during my research work. I was fortunate enough to undertake it in three outstanding laboratories, with inspiring supervisors and coworkers as a PhD student and postdoc, then with talented and enthusiastic colleagues and students since my arrival in the Quantronics group at CEA Saclay.

5.1 Concluding remarks

Working during my PhD in cavity QED with Rydberg atoms was an opportunity to acquire an intuition about the most fundamental aspects of quantum physics, while getting hands-on training on a demanding experimental setup. We used Rydberg atoms to generate one of the simplest non-classical states of the field in a microwave cavity, the one-photon Fock state; we then measured its Wigner function and revealed its negativity around the center of phase space [2]. The lifetime of the cavity field was so short in our experiment that we had to resort to a trick which consisted in using the same atom to both prepare the cavity field and measure it; otherwise the field would have already relaxed to the vacuum if probed by a subsequent atom. After the end of my PhD the quality factor of the microwave cavity was improved by two orders of magnitude thanks to the group efforts, so that the photon number could stay unchanged during the passage of several successive atoms. This made it possible to push the quantum state engineering and probing of the field by the Rydberg atoms to a completely new level, with in particular the first direct observation of the quantum trajectories of the photon number in the cavity [18], a milestone for quantum optics and quantum physics in general.

At the time of my PhD, the only experiments reaching the celebrated "strong coupling" regime necessary to generate entangled states of several particles were atomic cavity QED [107] and trapped-ion experiments [31], which encompassed essentially 5 research groups in the world; manipulating the quantum state of individual coupled quantum systems was restricted to these complex atomic physics experimental setups. I was thus immensely surprised when it became clear that the superconducting flux-qubit circuit that we were measuring during my postdoc in Delft in 2003 was in fact strongly coupled to a parasitic on-chip resonance, and that we could easily drive their joint quantum state with sideband transitions in complete analogy with trapped-ion experiments [3]. Whereas our discovery was not planned, the group of R. Schoelkopf at Yale University had designed a dedicated experiment which led

to the first observation of the vacuum Rabi splitting in a superconducting qubit coupled to a coplanar resonator [4]. The combination of the two results marked the birth of circuit QED and the extension of superconducting qubit research into the realm of quantum optics, which resulted in a strong broadening of the scientific community working on the quantum state engineering of indivdual coupled systems. Vacuum Rabi splittings are nowadays straightforwardly observed in many research groups, and more generally all the concepts and ideas developed in cavity QED [17] have been vigorously disseminated throughout the mesoscopic physics community.

One of the remarkable aspects of circuit QED is the dispersive readout of the qubit state via the cavity [47]. In Saclay we made use of this variable-strength quantum non-destructive measurement to conduct fundamental investigations of the measurement back-action in quantum mechanics. Motivated by a series of predictions of A. Korotkov, we performed an experiment in which a two-level system is submitted to the conflicting actions of a continuous drive, which induces quantum coherent oscillations between the two basis states, and of a continuous projective readout which tends to project the qubit onto one of these states. This research program culminated with the first test and violation of the Leggett-Garg inequality, proving that superconducting circuits do behave quantum-mechanically despite their macroscopic character [7]. The next step was taken by other groups [57, 58]: using the signal from the continuous qubit monitoring to react on the qubit dynamics and actively stabilize the phase of its coherent oscillations. These quantum feedback schemes [108] became only possible after quantum-limited amplifiers at microwave frequencies were developed [109, 110]. The importance of these parametric amplifiers for the future of the field can hardly be over-estimated, since they enable for the first time microwave signals to be measured at the shot-noise limit, and puts therefore quantum optics in the microwave domain on the same footing as in the optical domain.

Besides fundamental quantum physics experiments, circuit QED is also actively investigated as an architecture for quantum information processing [46], and a strong worldwide effort is dedicated to using and perfecting the qubit circuits for building an actual quantum computer. Our contribution was to realize the first high-fidelity transmon qubit readout in circuit QED [111], and to demonstrate quantum speed-up with an elementary two-qubit processor [112, 113]. Recent progress of qubit coherence times [37, 39, 114], obtained thanks to many systematic studies and improvements of sample fabrication as well as the measurement setup, puts indeed superconducting qubits among the strongest candidates for implementing quantum computation [115, 116, 117]; and experiments with small-scale quantum processors of order 10 qubits are for sure within reach on a short timescale. The major challenge nowadays is the demonstration of a qubit actively protected against computational errors.

5.2 Future projects : circuit QED with spins

If our group has a strong activity in superconducting quantum computing with in particular the PhD thesis of V. Schmitt aiming at the demonstration of a scalable 4-qubit quantum processor, my present research interests have however somewhat shifted aside that goal. I am now and for the foreseeable future dedicated to explore and develop the links between quantum spin dynamics and circuit QED, which I

believe are numerous and yet to be discovered.

In this manuscript I have described our most advanced project in that area: the realization of an operational quantum memory based on ensembles of NV centers in diamond [105], able to store the state of multiple qubits over long times and to retrieve them on-demand. Since the beginning of the project in 2009, several results obtained in the group (in particular by Yuimaru Kubo and Cécile Grezes during her PhD) indicate the feasability of this idea [14, 15].

Another project, conducted by Audrey Bienfait as a PhD and Michaël Stern as postdoc, aims at developing circuit QED with single spins instead of large ensembles. Several motivations make this an attractive goal. Quantum information with spin qubits made important progress in the recent years, with several new experiments demonstrating the readout and manipulation of individual nuclear and electron spins [118, 119, 120], and the experimental demonstration of remarkably long coherence times (up to 30 s for an individual nuclear spin in silicon [121]). Although impressive experiments have very recently reported the entanglement [90] and teleportation [122] of distant NV centers based on the measurement of optical photons emitted by each NV, finding efficient schemes for entangling distant spins remains one of the main challenges of spin-qubit research.

Superconducting circuits would constitute ideal quantum buses to mediate the interaction between distant spins by exchange of real or virtual microwave photons; the combination of circuit QED and of single spin manipulation and readout could result in an operational spin-qubit architecture for quantum information processing. Another motivation is the interest of pushing electron spin resonance sensitivity up to the single spin limit, which could have applications to single-molecule science. As mentioned in this manuscript, reaching the strong coupling of a single electronic spin with microwave photons in a cavity is unfortunately very challenging due to the small value of the coupling constant; however, using optimized miniature resonators and circuits, this coupling strength could reach the necessary value. This would open the way to the development of single-spin circuit QED as a new field at the interface of microwave quantum optics and quantum spin dynamics.

Bibliography

[1] S. Osnaghi, P. Bertet, A. Auffeves, P. Maioli, M. Brune, J. M. Raimond, and S. Haroche, Phys. Rev. Lett. **87**, 037902 (2001).

[2] P. Bertet, A. Auffeves, P. Maioli, S. Osnaghi, T. Meunier, M. Brune, J. M. Raimond, and S. Haroche, Phys. Rev. Lett. **89**, 200402 (2002).

[3] I. Chiorescu, P. Bertet, K. Semba, Y. Nakamura, C. J. P. M. Harmans, and J. E. Mooij, Nature **431**, 159 (2004), ISSN 0028-0836.

[4] A. Wallraff, D. I. Schuster, A. Blais, L. Frunzio, R. Huang, J. Majer, S. Kumar, S. M. Girvin, and R. J. Schoelkopf, Nature **431**, 162 (2004).

[5] Y. Makhlin, G. Schoen, and A. Shnirman, Nature **431**, 138 (2004).

[6] P. Bertet, I. Chiorescu, G. Burkard, K. Semba, C. J. P. M. Harmans, D. P. DiVincenzo, and J. E. Mooij, Phys. Rev. Lett. **95**, 257002 (2005).

[7] A. Palacios-Laloy, F. Mallet, F. Nguyen, P. Bertet, D. Vion, D. Esteve, and A. N. Korotkov, Nature Physics **6**, 442 (2010), ISSN 1745-2473.

[8] A. Palacios-Laloy, Ph.D. thesis (2010).

[9] I. Siddiqi, R. Vijay, F. Pierre, C.M.Wilson, M. Metcalfe, C. Rigetti, L. Frunzio, and M. H. Devoret, Phys. Rev. Lett. **93**, 207002 (2004).

[10] A. Lupaşcu, S. Saito, T. Picot, P. De Groot, C. Harmans, and J. Mooij, Nature Physics **3**, 119 (2007).

[11] F. Mallet, F. Ong, A. Palacios-Laloy, F. Nguyen, P. Bertet, D. Vion, and D. Esteve, Nature Physics **5**, 791 (2009), ISSN 1745-2473.

[12] F. R. Ong, M. Boissonneault, F. Mallet, A. Palacios-Laloy, A. Dewes, A. C. Doherty, A. Blais, P. Bertet, D. Vion, and D. Esteve, Physical Review Letters **106**, 167002 (2011).

[13] F. R. Ong, M. Boissonneault, F. Mallet, A. C. Doherty, A. Blais, D. Vion, D. Esteve, and P. Bertet, Phys. Rev. Lett. **110**, 047001 (2013).

[14] Y. Kubo, F. R. Ong, P. Bertet, D. Vion, V. Jacques, D. Zheng, A. Dreau, J. F. Roch, A. Auffeves, F. Jelezko, et al., Phys. Rev. Lett. **105**, 140502 (2010).

[15] Y. Kubo, C. Grezes, A. Dewes, T. Umeda, J. Isoya, H. Sumiya, N. Morishita, H. Abe, S. Onoda, T. Ohshima, et al., Phys. Rev. Lett. **107**, 220501 (2011).

[16] Y. Kubo, I. Diniz, C. Grezes, T. Umeda, J. Isoya, H. Sumiya, T. Yamamoto, H. Abe, S. Onoda, T. Ohshima, et al., Phys. Rev. B **86**, 064514 (2012).

[17] S. Haroche and J.-M. Raimond, *Exploring the Quantum* (Oxford University Press, 2006).

[18] C. Guerlin, J. Bernu, S. Deleglise, C. Sayrin, S. Gleyzes, S. Kuhr, M. Brune, J.-M. Raimond, and S. Haroche, Nature **448**, 889 (2007), ISSN 0028-0836.

[19] D. T. Smithey, M. Beck, M. G. Raymer, and A. Faridani, Phys. Rev. Lett. **70**, 1244 (1993).

[20] G. Breitenbach, T. Müller, S. F. Pereira, J.-P. Poizat, S. Schiller, and J. Mlynek, J. Opt. Soc. Am. B **12**, 2304 (1995).

[21] L. G. Lutterbach and L. Davidovich, Phys. Rev. Lett. **78**, 2547 (1997).

[22] P. Bertet, Ph.D. thesis (2002).

[23] S. Deleglise, I. Dotsenko, C. Sayrin, J. Bernu, M. Brune, and J.-M. Raimond, Nature **455**, 510 (2008).

[24] M. Hofheinz, H. Wang, M. Ansmann, R. C. Bialczak, E. Lucero, M. Neeley, A. D. O'Connell, D. Sank, J. Wenner, J. M. Martinis, et al., Nature **459**, 546 (2009), ISSN 0028-0836.

[25] Y. Nakamura, Y. Pashkin, and J.-S. Tsai, Nature **398**, 786 (1999).

[26] J. E. Mooij, T. P. Orlando, L. Levitov, L. Tian, C. H. van der Wal, and S. Lloyd, Science **285**, 1036 (1999).

[27] C. H. van der Wal, A. C. J. ter Haar, F. K. Wilhelm, R. N. Schouten, C. J. P. M. Harmans, T. P. Orlando, S. Lloyd, and J. E. Mooij, Science **290**, 773 (2000).

[28] D. Vion, A. Aassime, A. Cottet, P. Joyez, H. Pothier, C. Urbina, D. Esteve, and M. H. Devoret, Science **296**, 886 (2002).

[29] I. Chiorescu, Y. Nakamura, C. J. P. M. Harmans, and J. E. Mooij, Science **299**, 1869 (2003).

[30] P. Bertet, I. Chiorescu, C. Harmans, and J. Mooij, arXiv:cond-mat/0507290 (2005).

[31] D. Leibfried, R. Blatt, C. Monroe, and D. Wineland, Rev. Mod. Phys. **75**, 281 (2003).

[32] P. Bertet, C. J. P. M. Harmans, and J. E. Mooij, Phys. Rev. B **73**, 064512 (2006).

[33] M. C. Goorden, M. Thorwart, and M. Grifoni, Phys. Rev. Lett. **93**, 267005 (2004).

[34] A. Wallraff, D. I. Schuster, A. Blais, J. M. Gambetta, J. Schreier, L. Frunzio, M. H. Devoret, S. M. Girvin, and R. J. Schoelkopf, Phys. Rev. Lett. **99**, 050501 (2007).

[35] P. J. Leek, M. Baur, J. M. Fink, R. Bianchetti, L. Steffen, S. Filipp, and A. Wallraff, Phys. Rev. Lett. **104**, 100504 (2010).

[36] I. Siddiqi, R. Vijay, M. Metcalfe, E. Boaknin, L. Frunzio, R. J. Schoelkopf, and M. H. Devoret, Phys. Rev. B **73**, 054510 (2006).

[37] H. Paik, D. I. Schuster, L. S. Bishop, G. Kirchmair, G. Catelani, A. P. Sears, B. R. Johnson, M. J. Reagor, L. Frunzio, L. I. Glazman, et al., Phys. Rev. Lett. **107**, 240501 (2011).

[38] A. P. Sears, A. Petrenko, G. Catelani, L. Sun, H. Paik, G. Kirchmair, L. Frunzio, L. I. Glazman, S. M. Girvin, and R. J. Schoelkopf, Phys. Rev. B **86**, 180504 (2012).

[39] C. Rigetti, J. M. Gambetta, S. Poletto, B. L. T. Plourde, J. M. Chow, A. D. Córcoles, J. A. Smolin, S. T. Merkel, J. R. Rozen, G. A. Keefe, et al., Phys. Rev. B **86**, 100506 (2012).

[40] J. Bylander, S. Gustavsson, F. Yan, F. Yoshihara, K. Harrabi, G. Fitch, D. Cory, Y. Nakamura, J.-T. Tsai, and W. Oliver, Nat. Phys. **7**, 565 (2011).

[41] F. G. Paauw, A. Fedorov, C. J. P. M. Harmans, and J. E. Mooij, Phys. Rev. Lett. **102**, 090501 (2009).

[42] D. Marcos, M. Wubs, J. M. Taylor, R. Aguado, M. D. Lukin, and A. S. Sørensen, Phys. Rev. Lett. **105**, 210501 (2010).

[43] X. Zhu, S. Saito, A. Kemp, K. Kakuyanagi, S.-i. Karimoto, H. Nakano, W. J. Munro, Y. Tokura, M. S. Everitt, K. Nemoto, et al., Nature **478**, 221 (2011), ISSN 0028-0836.

[44] M. Stern, Y. Kubo, C. Grezes, A. Bienfait, D. Vion, D. Esteve, and P. Bertet, arxiv:1403.3871 (2014).

[45] A. J. Leggett and A. Garg, Phys. Rev. Lett. **54**, 857 (1985).

[46] A. Blais, R. Huang, A. Wallraff, S. M. Girvin, and R. J. Schoelkopf, Phys. Rev. A **69**, 062320 (2004).

[47] A. Wallraff, D. I. Schuster, A. Blais, L. Frunzio, J. Majer, M. H. Devoret, S. M. Girvin, and R. J. Schoelkopf, Phys. Rev. Lett. **95**, 060501 (2005).

[48] J. Koch, T. M. Yu, J. Gambetta, A. A. Houck, D. I. Schuster, J. Majer, A. Blais, M. H. Devoret, S. M. Girvin, and R. J. Schoelkopf, Phys. Rev. A **76**, 042319 (2007).

[49] J. A. Schreier, A. A. Houck, J. Koch, D. I. Schuster, B. R. Johnson, J. M. Chow, J. M. Gambetta, J. Majer, L. Frunzio, M. H. Devoret, et al., Phys. Rev. B **77**, 180502(R) (2008).

[50] M. Devoret, B. Huard, R. Schoelkopf, and L. Cugliandolo, eds., *Quantum Machines - Measurement and Control of Engineered Quantum Systems: Lecture Notes of the Les Houches Summer Schools, volume 96* (Oxford University Press, 2013).

[51] H. M. Wiseman and G. J. Milburn, Phys. Rev. A **47**, 642 (1993).

[52] A. N. Korotkov and D. V. Averin, Phys. Rev. B **64**, 165310 (2001).

[53] A. N. Korotkov, Phys. Rev. B **60**, 5737 (1999).

[54] R. Ruskov, A. N. Korotkov, and A. Mizel, Phys. Rev. Lett. **96**, 200404 (2006).

[55] R. Ruskov and A. N. Korotkov, Phys. Rev. B **66**, 041401 (2002).

[56] A. N. Korotkov, Phys. Rev. B **71**, 201305 (2005).

[57] R. Vijay, C. Macklin, D. Slichter, S. Weber, K. Murch, R. Naik, A. Korotkov, and I. Siddiqi, Nature **490**, 77 (2012).

[58] P. Campagne-Ibarcq, E. Flurin, N. Roch, D. Darson, P. Morfin, M. Mirrahimi, M. H. Devoret, F. Mallet, and B. Huard, Phys. Rev. X **3**, 021008 (2013).

[59] J. Gambetta, A. Blais, M. Boissonneault, A. A. Houck, D. I. Schuster, and S. M. Girvin, Phys. Rev. A **77**, 012112 (2008).

[60] D. I. Schuster, A. P. Sears, E. Ginossar, L. DiCarlo, L. Frunzio, J. J. L. Morton, H. Wu, G. A. D. Briggs, B. B. Buckley, D. D. Awschalom, et al., Phys. Rev. Lett. **105**, 140501 (2010).

[61] J. E. Mooij, Nature Physics **6**, 401 (2010).

[62] M. Ansmann, H. Wang, R. C. Bialczak, M. Hofheinz, E. Lucero, M. Neeley, A. D. O'Connell, D. Sank, M. Weides, J. Wenner, et al., Nature **461**, 504 (2009).

[63] C. Emary, N. Lambert, and F. Nori, Reports on Progress in Physics **77**, 016001 (2014).

[64] G. C. Knee, S. Simmons, E. M. Gauger, J. J. Morton, H. Riemann, N. V. Abrosimov, P. Becker, H.-J. Pohl, K. M. Itoh, M. L. Thewalt, et al., Nature communications **3**, 606 (2012).

[65] R. E. George, L. M. Robledo, O. J. Maroney, M. S. Blok, H. Bernien, M. L. Markham, D. J. Twitchen, J. J. Morton, G. A. D. Briggs, and R. Hanson, Proceedings of the National Academy of Sciences **110**, 3777 (2013).

[66] G. Waldherr, P. Neumann, S. F. Huelga, F. Jelezko, and J. Wrachtrup, Phys. Rev. Lett. **107**, 090401 (2011).

[67] N. S. Williams and A. N. Jordan, Phys. Rev. Lett. **100**, 026804 (2008).

[68] M. E. Goggin, M. P. Almeida, M. Barbieri, B. P. Lanyon, J. L. O'Brien, A. G. White, and G. J. Pryde, Proceedings of the National Academy of Sciences **108**, 1256 (2011).

[69] J. P. Groen, D. Ristè, L. Tornberg, J. Cramer, P. C. de Groot, T. Picot, G. Johansson, and L. DiCarlo, Phys. Rev. Lett. **111**, 090506 (2013).

[70] K. Murch, S. Weber, C. Macklin, and I. Siddiqi, Nature **502**, 211 (2013).

[71] L. Tian, P. Rabl, R. Blatt, and P. Zoller, Phys. Rev. Lett. **92**, 247902 (2004).

[72] A. S. Sørensen, C. H. van der Wal, L. I. Childress, and M. D. Lukin, Phys. Rev. Lett. **92**, 063601 (2004).

[73] D. Petrosyan, G. Bensky, G. Kurizki, I. Mazets, J. Majer, and J. Schmiedmayer, Phys. Rev. A **79**, 040304 (2009).

[74] M. Hafezi, Z. Kim, S. L. Rolston, L. A. Orozco, B. L. Lev, and J. M. Taylor, Phys. Rev. A **85**, 020302 (2012).

[75] P. Rabl, D. DeMille, J. M. Doyle, M. D. Lukin, R. J. Schoelkopf, and P. Zoller, Phys. Rev. Lett. **97**, 033003 (2006).

[76] D. I. Schuster, A. Fragner, M. I. Dykman, S. A. Lyon, and R. J. Schoelkopf, Phys. Rev. Lett. **105**, 040503 (2010).

[77] A. Imamoglu, Phys. Rev. Lett. **102**, 083602 (2009).

[78] J. H. Wesenberg, A. Ardavan, G. A. D. Briggs, J. J. L. Morton, R. J. Schoelkopf, D. I. Schuster, and K. Mølmer, Phys. Rev. Lett. **103**, 070502 (2009).

[79] T. Nirrengarten, A. Qarry, C. Roux, A. Emmert, G. Nogues, M. Brune, J.-M. Raimond, and S. Haroche, Phys. Rev. Lett. **97**, 200405 (2006).

[80] S. Bernon, H. Hattermann, D. Bothner, M. Knufinke, P. Weiss, F. Jessen, D. Cano, M. Kemmler, R. Kleiner, D. Koelle, et al., Nature communications **4**, 2380 (2013).

[81] S. D. Hogan, J. A. Agner, F. Merkt, T. Thiele, S. Filipp, and A. Wallraff, Phys. Rev. Lett. **108**, 063004 (2012).

[82] K. Petersson, L. McFaul, M. Schroer, M. Jung, J. Taylor, A. Houck, and J. Petta, Nature **490**, 380 (2012).

[83] A. D. O'Connell, M. Hofheinz, M. Ansmann, R. C. Bialczak, M. Lenander, E. Lucero, M. Neeley, D. Sank, H. Wang, M. Weides, et al., Nature **464**, 697 (2010).

[84] J.-M. Pirkkalainen, S. Cho, J. Li, G. Paraoanu, P. Hakonen, and M. Sillanpää, Nature **494**, 211 (2013).

[85] G. Balasubramian, P. Neumann, D. Twitchen, M. Markham, R. Koselov, N. Mizuochi, J. Isoya, J. Achard, J. Beck, J. Tissler, et al., Nature Materials **8**, 383 (2009).

[86] N. Bar-Gill, L. Pham, A. Jarmola, D. Budker, and R. Walsworth, Nature Communications **4**, 1743 (2013).

[87] P. Neumann, R. Kolesov, V. Jacques, J. Beck, J. Tisler, A. Batalov, L. Rogers, N. B. Manson, G. Balasubramanian, F. Jelezko, et al., New Journal of Physics **11**, 013017 (2009).

[88] L. Robledo, L. Childress, H. Bernien, B. Hensen, P. Alkemade, and R. Hanson, Nature **477**, 574 (2011).

[89] F. Jelezko, T. Gaebel, I. Popa, A. Gruber, and J. Wrachtrup, Phys. Rev. Lett. **92**, 076401 (2004).

[90] H. Bernien, B. Hensen, W. Pfaff, G. Koolstra, M. Blok, L. Robledo, T. Taminiau, M. Markham, D. Twitchen, and R. Hanson, Nature **497**, 86 (2013).

[91] J. Taylor, P. Cappellaro, L. Childress, L. Jiang, P. Hemmer, A. Yacoby, R. Walsworth, and M. Lukin, Nature Physics **4**, 810 (2008).

[92] A. Dréau, P. Spinicelli, J. R. Maze, J.-F. Roch, and V. Jacques, Phys. Rev. Lett. **110**, 060502 (2013).

[93] L. Rondin, J.-P. Tetienne, S. Rohart, A. Thiaville, T. Hingant, P. Spinicelli, J.-F. Roch, and V. Jacques, Nature Communications **4**, 2279 (2013).

[94] P. Maurer, G. Kucsko, C. Latta, L. Jiang, N. Yao, S. Bennett, F. Pastawski, D. Hunger, N. Chrisholm, M. Markham, et al., Science **336**, 1283 (2012).

[95] M. G. Raizen, R. J. Thompson, R. J. Brecha, H. J. Kimble, and H. J. Carmichael, Phys. Rev. Lett. **63**, 240 (1989).

[96] J. M. Fink, R. Bianchetti, M. Baur, M. Göppl, L. Steffen, S. Filipp, P. J. Leek, A. Blais, and A. Wallraff, Phys. Rev. Lett. **103**, 083601 (2009).

[97] Y. Kaluzny, P. Goy, M. Gross, J. M. Raimond, and S. Haroche, Phys. Rev. Lett. **51**, 1175 (1983).

[98] I. Diniz, S. Portolan, R. Ferreira, J. M. Gérard, P. Bertet, and A. Auffèves, Phys. Rev. A **84**, 063810 (2011).

[99] Z. Kurucz, J. H. Wesenberg, and K. Mølmer, Phys. Rev. A **83**, 053852 (2011).

[100] A. Palacios-Laloy, F. Nguyen, F. Mallet, P. Bertet, D. Vion, and D. Esteve, J. Low Temp. Phys. **151**, 1034 (2008).

[101] R. Amsüss, C. Koller, T. Nöbauer, S. Putz, S. Rotter, K. Sandner, S. Schneider, M. Schramböck, G. Steinhauser, H. Ritsch, et al., Phys. Rev. Lett. **107**, 060502 (2011).

[102] V. Ranjan, G. de Lange, R. Schutjens, T. Debelhoir, J. P. Groen, D. Szombati, D. J. Thoen, T. M. Klapwijk, R. Hanson, and L. DiCarlo, Phys. Rev. Lett. **110**, 067004 (2013).

[103] S. Probst, H. Rotzinger, S. Wünsch, P. Jung, M. Jerger, M. Siegel, A. V. Ustinov, and P. A. Bushev, Phys. Rev. Lett. **110**, 157001 (2013).

[104] Y. Kubo, I. Diniz, A. Dewes, V. Jacques, A. Dréau, J.-F. Roch, A. Auffeves, D. Vion, D. Esteve, and P. Bertet, Phys. Rev. A **85**, 012333 (2012).

[105] B. Julsgaard, C. Grezes, P. Bertet, and K. Mølmer, Phys. Rev. Lett. **110**, 250503 (2013).

[106] C. Grezes, B. Julsgaard, Y. Kubo, M. Stern, T. Umeda, J. Isoya, H. Sumiya, S. Abe, S. Onoda, T. Ohshima, et al., arXiv:1401.7939v1 (2014).

[107] J. M. Raimond, M. Brune, and S. Haroche, Rev. Mod. Phys. **73**, 565 (2001).

[108] D. Ristè, C. C. Bultink, K. W. Lehnert, and L. DiCarlo, Phys. Rev. Lett. **109**, 240502 (2012).

[109] M. A. Castellanos-Beltran and K. W. Lehnert, Appl. Phys. Lett. **91**, 083509 (2007).

[110] N. Bergeal, F. Schackert, M. Metcalfe, R. Vijay, V. E. Manucharyan, L. Frunzio, D. E. Prober, R. J. Schoelkopf, S. M. Girvin, and M. H. Devoret, Nature **465**, 64 (2010), ISSN 0028-0836.

[111] F. Mallet, F. R. Ong, A. Palacios-Laloy, F. Nguyen, P. Bertet, D. Vion, and D. Esteve, Nature Phys. **5**, 791 (2009).

[112] A. Dewes, F. R. Ong, V. Schmitt, R. Lauro, N. Boulant, P. Bertet, D. Vion, and D. Esteve, Phys. Rev. Lett. **108**, 057002 (2012).

[113] A. Dewes, R. Lauro, F. R. Ong, V. Schmitt, P. Milman, P. Bertet, D. Vion, and D. Esteve, Phys. Rev. B **85**, 140503 (2012).

[114] R. Barends, J. Kelly, A. Megrant, D. Sank, E. Jeffrey, Y. Chen, Y. Yin, B. Chiaro, J. Mutus, C. Neill, et al., Phys. Rev. Lett. **111**, 080502 (2013).

[115] M. Reed, L. DiCarlo, S. Nigg, L. Sun, L. Frunzio, S. Girvin, and R. Schoelkopf, Nature **482**, 382 (2012).

[116] L. Steffen, Y. Salathe, M. Oppliger, P. Kurpiers, M. Baur, C. Lang, C. Eichler, G. Puebla-Hellmann, A. Fedorov, and A. Wallraff, Nature **500**, 319 (2013).

[117] R. Barends, J. Kelly, A. Megrant, A. Veitia, D. Sank, E. Jeffrey, T. White, J. Mutus, A. Fowler, B. Campbell, et al., Nature **508**, 500 (2014).

[118] R. Vincent, S. Klyatskaya, M. Ruben, W. Wernsdorfer, and F. Balestro, Nature **488**, 357 (2012).

[119] S. Thiele, R. Vincent, M. Holzmann, S. Klyatskaya, M. Ruben, F. Balestro, and W. Wernsdorfer, Physical review letters **111**, 037203 (2013).

[120] A. Morello, J. J. Pla, F. A. Zwanenburg, K. W. Chan, K. Y. Tan, H. Huebl, M. Möttönen, C. D. Nugroho, C. Yang, J. A. van Donkelaar, et al., Nature **467**, 687 (2010).

[121] J. T. Muhonen, J. P. Dehollain, A. Laucht, F. Hudson, T. Sekiguchi, K. Ioth, D. N. Jamieson, J. C. McCallum, A. S. Dzurak, and A. Morello, arXiv:1402.7140 (2014).

[122] W. Pfaff, H. Bernien, S. van Dam, M. Blok, T. Taminiau, M. Tiggelman, R. Schouten, M. Markham, D. Twitchen, and R. Hanson, arxiv:1404.4369 (2014).